

Lawrence Berkeley National Laboratory

LBL Publications

Title

Joint Geophysical and Numerical Insights of the Coupled Thermal-Hydro-Mechanical Processes During Heating in Salt

Permalink

<https://escholarship.org/uc/item/1db4c9nw>

Journal

Journal of Geophysical Research: Solid Earth, 128(9)

ISSN

2169-9313

Authors

Wang, Jiannan
Uhlemann, Sebastian
Otto, Shawn
et al.

Publication Date

2023-09-01

DOI

10.1029/2023jb026954

Copyright Information

This work is made available under the terms of a Creative Commons Attribution License, available at <https://creativecommons.org/licenses/by/4.0/>

Peer reviewed

JGR Solid Earth

RESEARCH ARTICLE

10.1029/2023JB026954

Key Points:

- We conducted in situ geophysical monitoring during a controlled heating experiment in salt formations
- While temperature effects explain resistivity changes near the heater well, more resistivity decreases were observed at the further regions
- Numerical simulations indicate pore pressure driven brine migration is likely the primary reason for the resistivity changes beyond temperature effects

Correspondence to:

J. Wang,
jiannanwang@lbl.gov

Citation:

Wang, J., Uhlemann, S., Otto, S., Dozier, B., Kuhlman, K. L., & Wu, Y. (2023). Joint geophysical and numerical insights of the coupled thermal-hydro-mechanical processes during heating in salt. *Journal of Geophysical Research: Solid Earth*, 128, e2023JB026954. <https://doi.org/10.1029/2023JB026954>

Received 21 APR 2023

Accepted 2 SEP 2023


Author Contributions:

Conceptualization: Jiannan Wang, Yuxin Wu
Data curation: Sebastian Uhlemann, Shawn Otto, Brian Dozier, Kristopher L. Kuhlman
Formal analysis: Sebastian Uhlemann
Funding acquisition: Yuxin Wu
Investigation: Jiannan Wang, Shawn Otto, Kristopher L. Kuhlman, Yuxin Wu
Methodology: Jiannan Wang, Yuxin Wu
Project Administration: Yuxin Wu
Resources: Brian Dozier, Yuxin Wu
Supervision: Yuxin Wu
Visualization: Jiannan Wang
Writing – original draft: Jiannan Wang

© 2023. The Authors.

This is an open access article under the terms of the [Creative Commons Attribution-NonCommercial-NoDerivs License](https://creativecommons.org/licenses/by-nc-nd/4.0/), which permits use and distribution in any medium, provided the original work is properly cited, the use is non-commercial and no modifications or adaptations are made.

Joint Geophysical and Numerical Insights of the Coupled Thermal-Hydro-Mechanical Processes During Heating in Salt

Jiannan Wang¹ , Sebastian Uhlemann¹ , Shawn Otto², Brian Dozier², Kristopher L. Kuhlman³ , and Yuxin Wu¹ 

¹Lawrence Berkeley National Laboratory, Berkeley, CA, USA, ²Los Alamos National Laboratory, Carlsbad, NM, USA,

³Sandia National Laboratories, Albuquerque, NM, USA

Abstract Salt offers an optimal medium for the permanent isolation of heat-producing radioactive waste due to its impermeability, high thermal conductivity, and ability to close fractures through creep. A thorough understanding of the thermal-hydrological-mechanical (THM) processes, encompassing brine migration, is fundamental for secure radioactive waste disposal within salt formations. At the Waste Isolation Pilot Plant (WIPP), we conducted joint in situ geophysical monitoring experiments during active heating to investigate brine migration near excavations. This experiment incorporated electrical resistivity tomography (ERT) alongside high-resolution fiber-optic-based distributed temperature sensing within a controlled heating experiment. Additionally, discrete element model (DEM) based numerical simulations were conducted to simulate THM processes during heating, providing a more mechanistic understanding of the coupled processes leading to the observed changes in geophysical measurements. During heating, resistivity shifts near the heater were reasonably explained by temperature effects. However, in more distant, cooler regions, the resistivity decrease exceeded predictions based solely on temperature. DEM simulations highlighted brine migration, propelled by pore pressure gradients, as the likely primary factor contributing to the additional resistivity decline beyond temperature effects. The comparison between the predicted ERT responses and observations was much improved when considering the effects of brine migration based on the DEM simulations. These geophysical and simulation findings shed light on brine migration in response to salt heating, enhancing our understanding of the coupled THM processes in salt for safe radioactive waste disposal.

Plain Language Summary Brine migration within a salt nuclear waste repository induces corrosion and the dissolution of radionuclides, influencing their safety. Understanding the impact of waste-generated heat on fluid dynamics and salt rock deformation is pivotal for the secure disposal of radioactive waste in salt formations. A controlled heating experiment at the Waste Isolation Pilot Plant, New Mexico, was monitored for geophysical changes, including formation resistivity and temperature. Numerical simulations modeled rock behaviors to elucidate the coupled Thermo-Hydro-Mechanical processes and their impacts on observed signals. While resistivity changes near the heater were adequately explained by temperature effects alone, more distant and cooler regions exhibited disproportionately larger resistivity decreases. Numerical simulations identified brine migration as the primary cause for this significant decrease, surpassing temperature effects. Incorporating brine migration effects in simulations substantially improved the prediction of resistivity changes. These findings highlight the role of joint geophysical monitoring and numerical simulations for mechanistic understanding of the coupled processes during heating, which is important for safe storage of nuclear waste in salt formations.

1. Introduction

Nuclear energy is a stable, reliable, and clean energy (in terms of CO₂ emission) source. However, radioactive waste disposal remains a challenge to nuclear energy applications. Spent nuclear fuel is thermally hot as well as highly radioactive, thus requiring remote handling, shielding, and safe disposal. As of 2018, there are around 2.8 million cubic meters (m³) of spent fuel in temporary storage (IAEA, 2018) worldwide, including 364,000 m³ in the United States, where the volume of spent nuclear fuel waste continues to increase without a clear path to disposal (Faybishenko et al., 2017).

Salt is an ideal repository for the permanent isolation of heat-generating radioactive waste due to its ultra-low permeability, high thermal conductivity, and self-healing capability (from creep closure) under typical repository

Writing – review & editing: Jiannan Wang, Sebastian Uhlemann, Kristopher L. Kuhlman

conditions (Hess et al., 1957; Kuhlman & Malama, 2013). In addition, the high thermal conductivity of the rock salt facilitates efficient dissipation of heat into the surrounding formation, resulting in lower repository temperatures at earlier periods than alternative disposal media (Acton, 1978). In the far field, the ultra-low permeability and porosity of the salt formations can provide an excellent natural barrier to contain radionuclides over the long term (10^4 – 10^6 years) (Ballentine & Burnard, 2002; Beauheim & Roberts, 2002; Kuhlman & Malama, 2013). However, the short-term response of salt in proximity to a heat source encompasses intricate coupled multi-physics phenomena, such as brine and gas flow, precipitation and dissolution of salt, thermal expansion and contraction of salt and brine, and salt creep. These near-field behaviors impact the initial conditions for large-scale and long-time simulations used to assess the long-term performance of a repository (Kuhlman et al., 2017). Specifically, the intragranular and intergranular brine inside the salt formations (Kuhlman & Malama, 2013; Larson, 2000) could be stimulated by the nuclear waste decay introduced heat, which could drive waste package corrosion and radionuclides dissolution, facilitating their transport. Therefore it is essential to better understand the thermal-hydrological-mechanical (THM) coupling process at the field scale and their effects on brine migration to improve the scientific basis for safe radioactive waste disposal in salt.

Both bedded and domal salt formations could be used for nuclear waste disposal. The bedded salt is relatively dry (typically less than 5% water content by volume) with brine between crystal interfaces and minor fractures (Guiltinan et al., 2020; Larson, 2000). Several studies on the brine migration process in the salt repository have been conducted at different underground research facilities during the past decades (Guiltinan et al., 2020). Oak Ridge National Laboratory conducted a series of borehole heater tests in bedded salt between 1965 and 1967, with both electrical and radioactive sources in Carey Salt Mine near Lyons, Kansas (Project Salt Vault) (Bradshaw & McClain, 1971; Kuhlman & Malama, 2013). The average brine content is 0.31 vol% for heated salt (within 15 cm from the heater) and 0.50 vol% for unheated salt (at least 0.6 m from the heater) (Kuhlman & Malama, 2013). These tests quantified the brine inflow to the borehole by measuring the humidity of the circulated dry N_2 gas. During the tests, significant increases of the brine inflow rate were observed when the power level was changed (both increased and decreased). These early tests first observed brine migration in response to heating and cooling at the field scale, including thermal pressurization. From 1977 to 1980, the Office of Nuclear Waste Isolation carried out a heated brine migration field experiment in domal salt (with approximately 0.022 wt% water content) at Avery Island, Louisiana (Krause, 1983; Kuhlman & Malama, 2013). Dissolved (Mg^{2+} ion) and stable-water isotope (deuterated water) tracers were used to monitor brine migration. Compared to the bedded salt heater test in Kansas (Bradshaw & McClain, 1971), much less brine was produced in domal salt (less than 40 g brine per borehole array). During the 200-day test, approximately half (10.55 g) of the total brine (21 g) was produced during the 6-day cooling period after the heater was shut down, which was suggested to be related to permeability increase due to the cooling-induced tensile fracturing of the rock salt (Kuhlman & Malama, 2013). Using dry N_2 gas, extended permeability experiments were performed in boreholes near the heater borehole (Blankenship & Stickney, 1983; Stickney & Van Sambeek, 1984). The in situ tests revealed that the permeability was lower in the hotter boreholes that were closer to the central heater by several orders of magnitude. This was attributed to the thermal expansion of the salt crystals, effectively closing off the inter-crystalline porosity associated with the excavation damaged zone (EDZ) of the access drift. The EDZ is defined as the salt proximate to excavations and includes fractures that may allow flow of gaseous and liquid water depending on their connectivity. The in situ tests at Avery Island indicated that salt permeability changes are strongly affected by the temperature gradient during the heater tests (Kuhlman & Malama, 2013). The tracer test indicated that thermal pressurization affected the intergranular brine transportation process, which correlated well with thermo-poroelasticity simulations (McTigue, 1986, 1990).

In the pursuit of comprehending macroscopic brine flow within heated salt, a sequence of laboratory experiments at the meter scale was conducted during the late 1970s and early 1980s by Sandia National Laboratories. These experiments utilized bedded salt sourced from potash mines near Carlsbad, NM (Lambert & Shefelbine, 1979). The laboratory experiments indicated that increasing heater power (from 28 to 200°C) led to increased brine inflow by a factor of 10 (from 0.2 ml/day to 3 ml/day). The water production rate peaked within 1–1.5 days from the beginning of the change. Mineralogical examination revealed the movement of intragranular fluid inclusions within sections of the salt block closest to the heating source, with minimal occurrence of migration across grain boundaries (Lambert, 1980). In addition, Lambert (1980) deduced that intragranular brine inclusions, upon encountering a grain boundary, have the potential to integrate into the intergranular fluid composition. However, using the same experimental results, Roedder and Bassett (1981) suggested that the intragranular brine inclusions

had not moved very far (the flow rate is about 1 cm/yr) and had not changed shape. Regardless of the disagreement between the two studies, both suggested that the intragranular brine migration mechanism was negligible during the active heating. However, intragranular brine may flow into the intergranular porosity, where it can flow under a liquid or gas pressure gradient. From 1985 to 1990, drift-scale heater tests were conducted at two different sets of temperatures (120 and 50°C) in vertical boreholes underground at Waste Isolation Pilot Plant (WIPP) (McTigue & Nowak, 1987; Nowak & McTigue, 1987). The experiments found that the hotter boreholes produced more brine (50–60 g/day per borehole) than cooler boreholes (9–10 g/day per borehole). Unfortunately, no brine inflow data were collected during the cool-down phase. In addition, the heterogeneity of the lithology also affects the brine inflow: The borehole with relatively purer halite did not produce brine, whereas the five boreholes intersected the 0.9-m anhydrite and clay layer, produced the most brine (150 kg of brine over 2 years).

These previous studies improved our understanding of the brine migration process in salt formations during heating. However, most of these observations were sparsely distributed with limited spatial resolution and coverage. The EDZ structure and brine migration pathways suggest that modern monitoring approaches with continuous and distributed in situ multi-geophysical observational tools can provide a more detailed view of the brine migration process in salt during heating. As part of the U.S. Department of Energy-Office of Nuclear Energy (DOE-NE) Spent Fuel and Waste Disposition field-testing campaign, this study focuses on the quantification of the transient evolution of brine inflow after excavating a drift or borehole as the initial conditions relevant to the long-term performance assessment of a generic salt repository system (P. J. Johnson et al., 2017; Kuhlman et al., 2017; Stauffer et al., 2015). In particular, the goal of the field test is to improve understanding of brine availability and its process in bedded salt, as well as collecting data sets for parameterizing numerical models. In this study, advanced geophysical monitoring was conducted during the Brine Availability Tests in Salt (BATS) experiments, where the in situ heating was conducted in horizontal boreholes in the WIPP underground. Three-dimensional (3D) electrical resistivity tomography (ERT) and high-resolution fiber-optic distributed temperature sensing (DTS) were conducted to study the spatial and temporal dynamics of the brine movement and the temperature evolution near the heat source. ERT has proven sensitivity to changes of rock temperature, formation porosity and permeability, and brine content, while fiber-optic DTS can provide high-resolution temperature profile at a millimeter scale over time. To better understand the mechanistic processes driving the observed geophysical signals, numerical simulations based on the discrete element model (DEM) were conducted to help understand the THM behaviors of the salt, the associate brine migration mechanism, and the observed ERT and DTS signals.

2. Materials and Methods

2.1. Site Description

Starting from 21 January 2020, a set of in situ heating experiments, BATS, was conducted at the WIPP underground facility in New Mexico. The WIPP repository is located inside the 600-m thick Permian Salado Formation. The experiment was conducted at 650 m below the surface (Figure 1a). X-ray CT, with Toshiba Aquilion TSX-101A/R medical CT scanner at a sub-millimeter core-scale resolution (430 μm by 430 μm by 500 μm), analyses from the retrieved core samplings during borehole drilling indicated that volumetrically 95.3%–97.7% of the rock is halite, with polyhalite (a hydrous sulfate mineral) comprising most of the remainder of the core (Better et al., 2020). This suggests that the geological salt formation at the experiment site can be considered almost homogeneous in terms of chemical composition, thermal conductivity, and mechanical properties.

2.2. In Situ Experiment Setup

A comprehensive monitoring and characterization plan, including thermocouples, ERT, DTS, acoustic emission, mechanical deformation, gas chemistry, as well as brine sampling/quantification, was implemented during the BATS experiment. Only ERT and DTS results will be discussed here, and the schematic diagram of the relevant borehole layout is shown in Figure 1b. The deviations of the boreholes are small and westward. The three 550-cm ERT boreholes have less than 5 cm southwest-ward drift. The 910-cm fiber-optic borehole has less than 12 cm westward drift, whereas the 550-cm fiber-optic borehole has around 10 cm westward drift. The heater borehole also has a 10 cm southwest-ward drift. The largest central borehole (12 cm diameter) was used to house the heater behind an inflatable packer. A 750-W quartz lamp infrared heater was mounted on a steel pipe with a diameter of 2.5 cm. The total length of the heater unit is 61 cm, centered in the 71 cm space between two reflectors. The

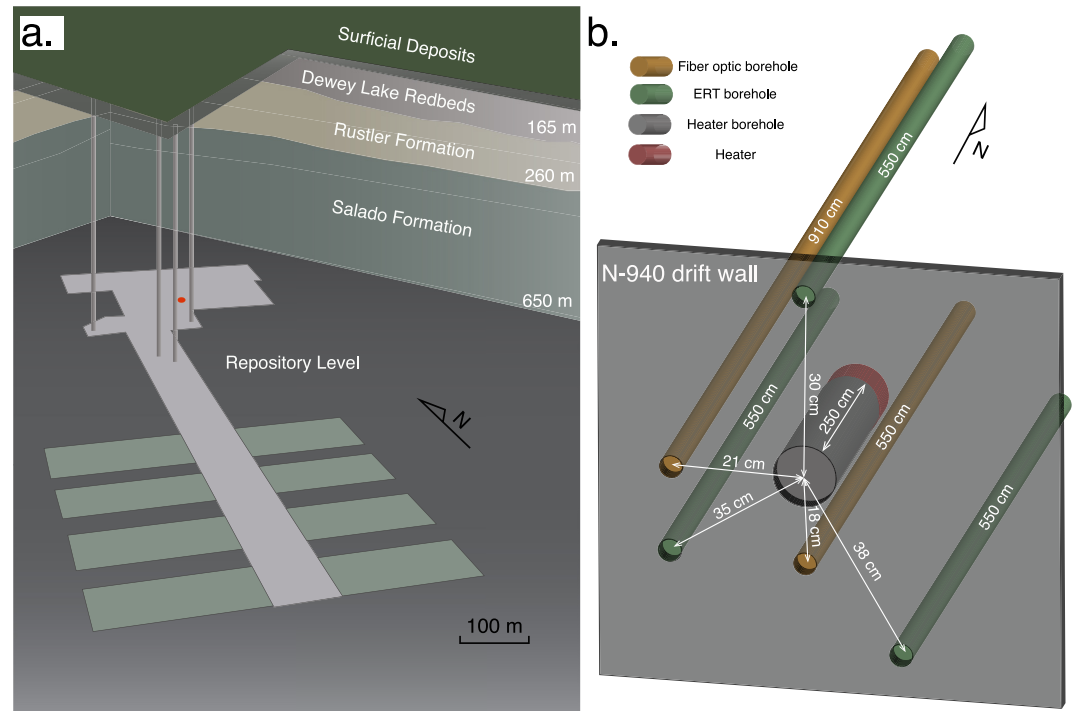


Figure 1. Electrical resistivity tomography (ERT) and distributed temperature sensing (DTS) configuration of the Brine Availability Tests in Salt experiment. (a) Schematic diagram of the geological setting of the Waste Isolation Pilot Plant repository. The red dot indicates the location of the in situ experiment test site (N-940). (b) Schematic diagram of the borehole layout at N-940 test site, showing the positions of the heater, ERT, and DTS boreholes.

heater was placed inside the horizontal heater borehole at 250 cm depth from the drift wall. The heater, controlled by a Watlow controller, was set at a constant temperature of 120°C during the initial heating phase. The Watlow controller output was transmitted to a Campbell Scientific CR1000X data logger. While our analysis is focused on the heated plot, we also monitored an unheated control plot with the identical borehole layout and instrumentation but without heating.

The first phase of the BATS experiment was conducted over a ~2-year period with multiple heating/cooling phases, tracer tests, and other characterization efforts. Here we focus our analysis on the ERT and DTS measurements during the initial heating phase from 21 January to 15 February 2020.

2.2.1. ERT Method

ERT is a geophysical method used to measure the resistivity distribution of the geological formation by injecting electrical current into the formation through pairs of electrodes and measuring the electrical potential distribution in the study domain (Reynolds, 2011). The resistivity distribution can be interpreted in terms of lithology, saturation, and other factors (Evangelista et al., 2017; Reynolds, 2011). During the BATS experiment, the lithology of the formation can be considered unchanged, making the measured resistivity changes closely related to temperature, microstructure, and pore fluid changes (i.e., brine migration) in the salt formation.

Three 5.5-m deep ERT boreholes with the diameter of 4.4 cm (green cylinders in Figure 1b) were completed for the experiments. Each of the ERT boreholes hosts 16 copper-ring electrodes (2.5 cm width) spaced 30 cm along each borehole. The electrodes were installed on the outside of the PVC conveyance pipes (1.9 cm ID, 2.5 cm OD), and connected by the wires through the inside of the pipes. For better coupling, the ERT boreholes are grouted both inside and outside of the PVC conveyance pipes. The electrodes were controlled by an ERT data acquisition system from Multi-Phase Technologies (MPT DAS-1), located inside an enclosure in the drift to minimize corrosion effects from salt dust. Inside each of the ERT boreholes, five thermocouples were installed for temperature measurements. The ERT electrode arrays were grouted into the boreholes via salt cement injection using the PVC conveyance pipes.

ERT data were acquired using a four-electrode setup: Two electrodes injected current into the salt formation, and two other electrodes measured the resulting electrical potential (voltage). Multiplexing of all 48 electrodes was carried out to acquire a tomographic data set for the monitoring domain, resulting in a total of 2,610 measurements for each data acquisition. Because the standard and most frequently used acquisition schemes, such as dipole-dipole or Wenner-type configurations, only provide a limited resolution within the studied domain (Loke et al., 2013), we used an optimized survey design adapted from Wilkinson et al. (2006) to achieve the best resolution and spatial coverage at reduced data acquisition time.

2.2.2. DTS Method

Distributed temperature sensing (DTS) during the experiment was carried out using a Rayleigh-based optical frequency domain reflectometry (OFDR) method, which utilizes backscattering of light due to the interference between the input light and naturally existing impurities with small refractive index variations along the entire fiber. The variation of the refractive index is unique for each fiber, which changes in response to external temperature or strain changes (Korganbayev et al., 2020). By analyzing the backscatter spectrum from each segment of the fiber, we can reconstruct the temperature or strain profile along the entire fiber. The fibers we used for experiment have the segment size (or gauge length) of 5.2 mm, with 50% overlapping, giving us the spatial resolution of 2.6 mm (Morra et al., 2020).

To acquire the detailed temperature profile during the heating experiment, two 4.4-cm diameter DTS boreholes were completed, with depths of 5.5 and 9.1 m, respectively (indicated by brown tubes in Figure 1b). The temperature fibers were housed inside 3-mm diameter plastic tubes to allow free sliding for protection and strain release from salt deformation. The fibers were attached to the outside of the PVC conveyance pipes and both were grouted into the borehole. In each of the DTS boreholes, four thermocouples were also grouted in with the fibers for temperature calibration and verification. After grouting, the fibers were well-coupled with the salt formation. Given that the temperature transients were relatively slow, the DTS sensors were sampled 10 times every hour. The DTS sensors were connected to an eight-channel Luna OFDR (ODiSI 6108), located in an enclosure in the drift. The thermocouples were read using a Campbell Scientific CR1000X data logger.

2.3. Numerical Simulation Method

While the in situ DTS and ERT measurements during the heating experiments provide valuable observations, they are indirect measurements of the brine migration THM process during heating. For example, the ERT measurements reveal an overall conductivity change, which is the result of multiple convoluted effects, including possible brine influx, saturation change, thermal-induced fracture creation/closure, temperature change as well as change of pore fluid ionic strength. The DTS measurements provide detailed temperature development inside the salt formation during the heating but lack information on hydrological and mechanical processes. Numerical modeling can be used to simulate the THM processes, such as pore pressure changes and thermal expansion, as well as a tool to link the geophysical measurements with the THM processes during the heating, such as temperature evolution and brine migration.

In this study, we used the discrete element method (DEM) to simulate the heating experiment at the WIPP. DEM is a numerical technique that calculates the interactions between many particles (Lee et al., 2017). Comparing to the continuum modeling approaches such as the finite element method or the finite difference method, DEM works better for discontinuous and highly deformable media such as packed or fluidized formation and granular materials (Caulk et al., 2020; Evans et al., 2009; Tomac & Gutierrez, 2015). In addition, the effective parameters influenced by micro- and mesoscale structural or multi-field alterations during the coupled thermal-mechanical process should be studied based on a micro or meso-based model (Wuttke et al., 2017). The modeling was implemented with the THMC model in Yade DEM open-source software (Caulk et al., 2020; Šmilauer et al., 2021). Several preceding studies have engaged in comparative analyses between DEM simulations of the THM process and alternative numerical simulation methodologies, alongside laboratory experiments. Caulk et al. (2020) conducted a comparative assessment between DEM simulations and the numerical simulation approach employed by Najari and Selvadurai (2014) using COMSOL, in conjunction with their laboratory experiment. This experimentation focused on scrutinizing cavity pressure variations within a granite rock sample during heating and cooling. The outcomes of the DEM simulation closely aligned with those of Najari and Selvadurai (2014), affirming their congruence. In a similar vein, Catalano et al. (2011) employed DEM to simulate fluid flow across a

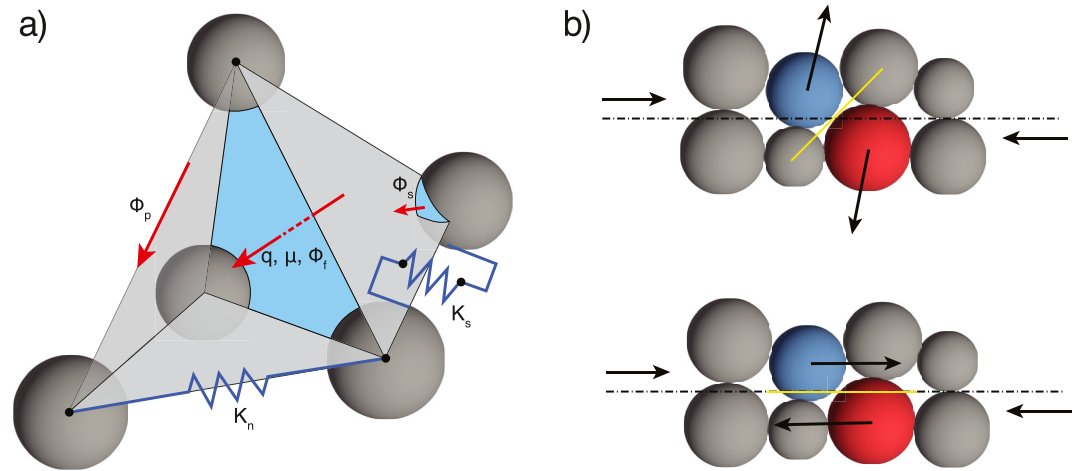


Figure 2. Schematic diagram of the heat transfer, fluid flow, and contact model. Modified from L. U. C. Scholtès and Donzé (2012) and Caulk et al. (2020). (a) Schematic diagram of the heat transfer, fluid flow, and contact model. (b) Schematic diagram of the joint contact logic before (top) and after (bottom) fracture. Φ_p represents the conductive heat flux between particles. Φ_s represents the conductive heat flux between solid and fluid. Φ_f represents the conductive heat flux within the fluid. μ represents the mass-energy flux. q represents the fluid flux. K_n and K_s represent the normal and shear stiffnesses between particles, respectively.

stationary solid skeleton. This simulation was juxtaposed against a prior laboratory experiment conducted by Wyllie and Gregory (1995) to evaluate permeability. The results showcased a robust concordance between the DEM-simulated outcomes and the experimental findings of Wyllie and Gregory (1995).

The mechanical scheme implemented in Yade integrates particle positions through time according to Newton's second law of motion. The DEM contact model follows the linear elastic model. The normal force between two interacting particles is evaluated according to normal stiffness and the displacement between particles (Caulk et al., 2020). Before the bond between the particles breaks, the stiffness is the bond stiffness. Similarly, the shear force between two interacting particles is evaluated according to shear stiffness and the displacement between particles. In addition, before the bond between particles breaks, the orientation of both particles also need to be considered. Upon the maximum displacement exceeding the rupture criteria, the normal stiffness is calculated from the stiffness of the contacting particles. The orientation of the shear force is re-oriented parallel to the fracture surface (L. U. C. Scholtès & Donzé, 2012). Utilizing the pore-finite volume (PFV) scheme, we capture the dynamics of compressible fluid flow within interstitial spaces among solid particles. The presented THM scheme integrates four distinct heat transfer models: a particle-to-particle conduction model, a particle-to-fluid conduction model, a fluid-to-fluid conduction model, and a heat advection model. Furthermore, the scheme incorporates thermo-mechanical couplings by accounting for the influences of both fluid thermal expansion and particle thermal expansion. For the thermo-hydro-mechanical coupling, the hydraulic force is decomposed into hydrostatic pressure and viscous shear stress, which are added to the inter-particle force estimation. The coupling between thermal and mechanical factors is via the thermal expansion and contraction of both the fluid and particles. This leads to alterations in pore volume, which are subsequently integrated into the ongoing volume changes. Figure 2 shows the schematic diagram of the PFV scheme, contact model as well as fracture joint contact logic used in this paper. A more detailed description and verification of the THMC implementation in Yade can be found in Caulk et al., 2020.

In DEM, the model is discretized into discrete elements (e.g., particles), which are mutually connected by deformable bonds (O'Sullivan, 2011). The macroscopic behavior of the model is influenced by both the microscopic parameters, such as stiffness, as well as the constitutive law. Simulations of macroscopic scale behaviors with the DEM do not need to reproduce the actual grain particle size because the interaction laws in the model are implemented as size independent. However, accurate macroscopic behavior simulation requires appropriate microscopic parameters. The microscopic parameters are usually identified via calibration against the experimental model, usually through the trial-and-error method, so that the macroscopic behavior of the model corresponds to the actual behavior as closely as possible (Stránský and Jirásek (2011)).

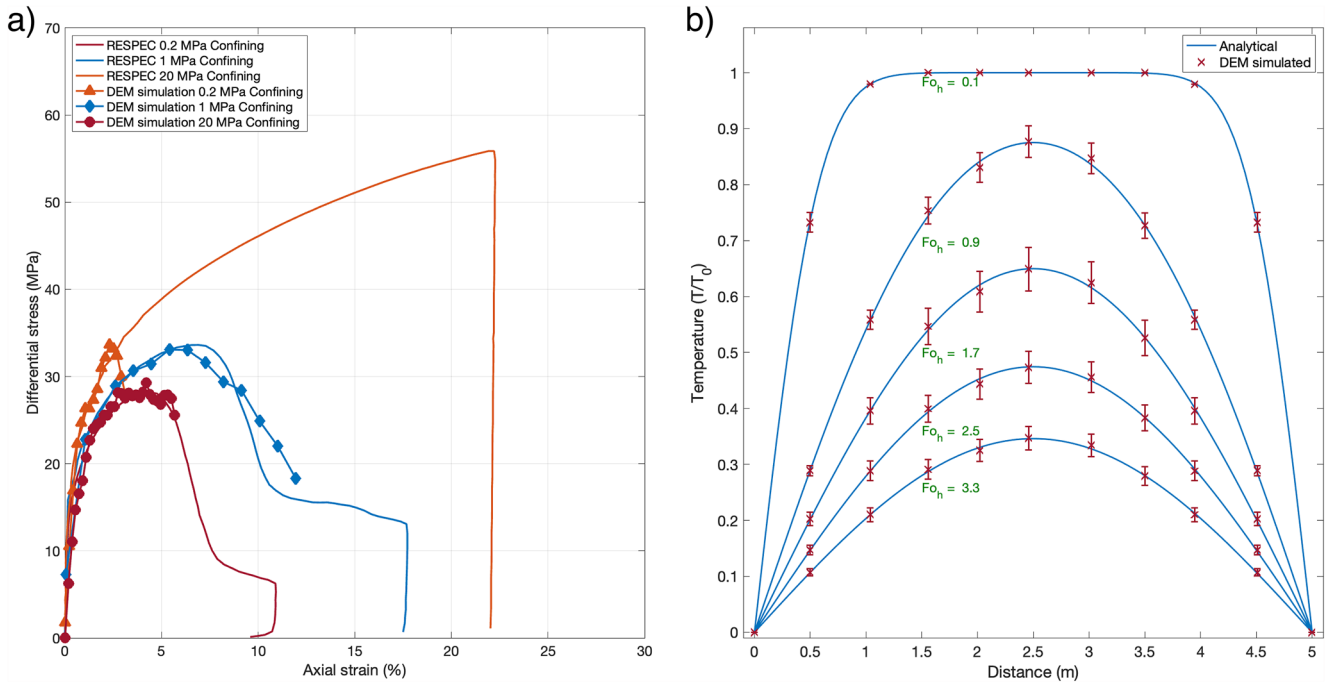


Figure 3. Discrete element model (DEM) calibration results. (a) DEM calibration against laboratory triaxial compression test (Buchholz, 2016). (b) Comparison of the evolution of temperature distribution between the random packing 5-m long rod DEM simulation and the analytical calculation from 1-D heat equation. Here, we use the Fourier number to characterize the thermal evolution process: $Fo_h = at/L^2$, where α is the effective thermal diffusivity ($\alpha = 6k_p/\pi C_p \rho_p$).

In this paper, the parameters used for the simulation were calibrated using triaxial compression tests, following the procedure in Caulk et al., 2020. The laboratory tests used for calibration were conducted by Buchholz (2016) with a clean rock salt sample from WIPP. During the calibration process, the micro DEM mechanical parameters, such as Young's modulus, Poisson's ratio, cohesion, and tensile strength, are adjusted to match the experimental curve. The calibrated results (Figure 3a) show good agreement between the numerical result and the lab test result when the differential stress is within 35 MPa, which is the suitable condition for our in situ test at WIPP. For the thermal diffusivity calibration, the DEM simulation a 5-m rod containing a random packing of 880 particles. This simulation was compared against the analytical solution for the 1D heat equation. Since the variation of effective thermal diffusivity comes from the random packing, we ran the simulation 50 times. In each simulation, the packing contains the same particle size distribution ($0.05 \text{ m} \pm 5\%$), but the particles were randomly positioned.

Consequently, different effective thermal diffusivity was used in the DEM simulation. The boundary particles were held at a consistent temperature ($T = 0^\circ\text{C}$), while the remaining particles were assigned a temperature of 120°C as the initial temperature. Figure 3b shows the calibration results. Conductive heat transfer results within DEM are within the anticipated statistical variance of the analytical solutions.

In order to lower the computation cost, we used density scaling to increase the time step without undermining the numerical stability. In DEM simulation, in order to maintain the numerical stability, we need to make sure the P -wave do not travel more than the minimum distance between two particles ($<2R$) within one time step. In addition, because of the interaction between the particles and boundary wall, the P -wave should not travel more than particle radius (R) within one time step. Hence, the critical time step (t_{cr}) can be written as:

$$t_{cr} = \min\left(R\sqrt{\frac{\rho}{E}}\right), \quad (1)$$

where R is the radius of the particle, ρ is the particle density, E is the Young's modulus. During the WIPP heating test, the process can be considered as quasi-static thermo-hydro-mechanical process, therefore, the movement of the particle is not our priority in this study. Given density only affects the particle velocity instead of the development of the particle force (Caulk et al., 2020), scaling density during the quasi-static state simulation can greatly

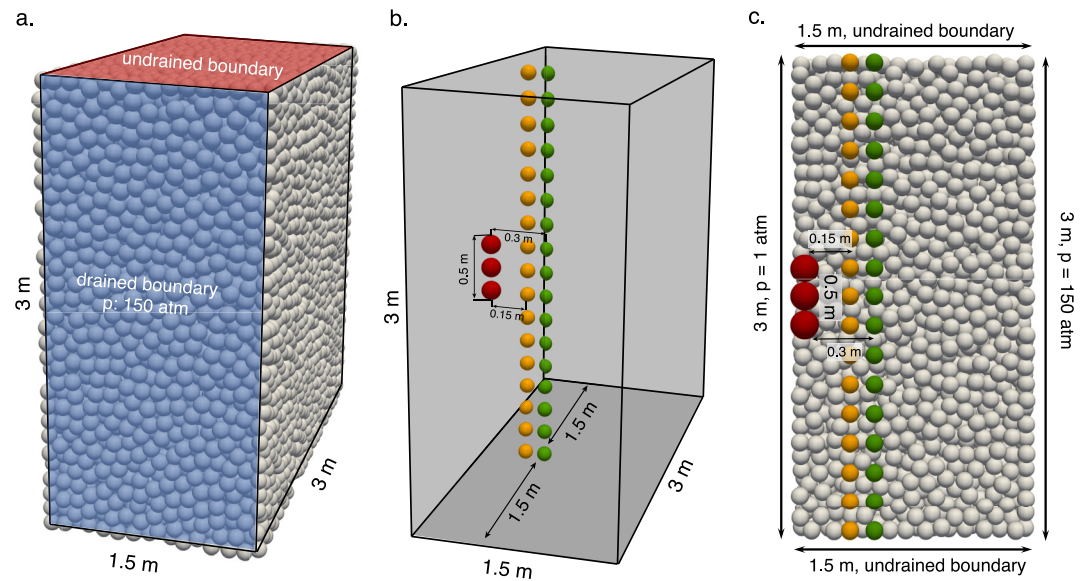


Figure 4. Discrete element model (DEM) numerical model. (a) The 1.5 m × 3 m × 3 m cube numerical model and the boundary conditions. (b) The locations of the heater array, fiber optic array, and electrical resistivity tomography (ERT) array. (c) The cross-section of the model and the boundary conditions. The red, yellow, and green particles represent the heater, the distributed temperature sensing borehole, and the ERT borehole used in the simulation, respectively.

reduce the computation cost. In this study, a density scaling factor of 10^{40} is employed, ensuring that the time step of 0.005 s remains stable without exerting any influence on the mechanical dynamics of the system.

After the DEM calibration, we set up the DEM model to emulate the heating test at WIPP. As described above, the heater was placed inside a borehole behind a packer. The packed-off interval was constantly purged with nitrogen gas to quantify brine production during the experiment. Therefore, the pressure applied to the wall inside the heater borehole is set to atmospheric pressure (101,325 Pa) in the DEM model. To properly simulate the boundary condition of the heater borehole as well as reduce the computation cost, we set up a half-space model with the heater on one side of the model with the open borehole boundary condition. As shown in Figure 4a, the model domain is 1.5 m × 3 m × 3 m, with the salt crystals represented as spherical particles averaged around 0.05 m in diameter. According to the salt sample, the grain size of the rock salt at WIPP range from 0.002 to 0.08 m in diameter. To achieve the balance between computation cost and simulation accuracy, we choose 0.05 m as the particle diameter in the DEM simulation. A previous study demonstrated that the utilization of 10,000 particles presents a good trade-off concerning computational efficiency and representativeness in behavior predictions. This quantity delineates the lower threshold beyond which the simulated macroscopic behavior attains independence from the model resolution, thereby ensuring its representativeness in behavior predictions (L. Scholtès & Donzé, 2013). In our model, the total particle number is more than 25,000. The heater, with a length of 0.5 m, is represented by three particles (each of which has the diameter of 0.16 m) and placed on one side of the model (indicated by the red particles in Figures 4b and 4c). The boundary with the heater is set at a constant fluid pressure of 101,325 Pa. Two linear arrays of particles, both consisting of 17 particles, represent the 5-m DTS borehole and the ERT borehole (Figures 4b and 4c). We focused on simulating the first 5 m of the 10-m DTS borehole, instead of the 5-m DTS borehole, because the first 5 m of the 10-m DTS measurement has less influence from the fiber dislocation and deformation (discussed later). Following the BATS experiment configuration (Figure 1b), the distance to the heater particle array from the DTS array and the ERT array is set at 0.2 and 0.3 m, respectively (Figures 4b and 4c). Given that the particle diameter is 0.05 m, we believe the location of the DTS array and the ERT array in the model reasonably represents the WIPP experiment configuration. The thermal conductivity changes with temperature. During the heating experiment at WIPP, the temperature was between 30 and 120°C. The laboratory experiment on the salt sample collected from WIPP indicates the thermal conductivity is around $4 \text{ W m}^{-1} \text{ K}^{-1}$ at such temperature range (Kuhlman et al., 2020). So, in the numerical simulation, we set the initial thermal conductivity to this value. The thermal and mechanical properties of the rock salt used in the simulation are shown in Table 1 (Chan et al., 1998; Guiltinan et al., 2020). After the heating started,

the borehole wall was kept at a constant temperature of 120°C. The initial temperature (except the heater) of the model is set at 28°C. According to the previous study (Guiltinan et al., 2020), the intact bedrock has a permeability of 10^{-21} m², whereas the damaged zone has 10^{-18} m². The site we conducted the in situ experiment involves both the damaged zone as well as the intact bedrock. Similarly, we used the same initial brine saturation of 90% for the salt formation as the previous study (Guiltinan et al., 2020). So, we used 5×10^{-19} m² as the average permeability of the model. The model is subject to an initial lithostatic pressure of 15 MPa (Chan et al., 1998). The hydraulic boundary conditions are shown in Figures 4b and 4c. The model is run under the no-heating condition until the pore pressure is equilibrated with 0.1-MPa pressure on the heater boundary and 15-MPa pressure on the opposite side of the model (Figure 4c), consistent with the baseline condition before heating started. The baseline pore pressure gradient after the pressure equilibration and before turning on the heater is shown in Figure 5.

3. Results

3.1. DTS Measurements at WIPP

The OFDR-based DTS system records the frequency shifts of the returned signals due to the temperature-induced changes on the fiber. To get the correct temperature, the records from the DTS were calibrated to the thermocouple measurements in the same boreholes. For both DTS boreholes, there are ~1 m of fiber exposed outside the boreholes. Data originating from the fibers that were laid outside of the borehole were omitted due to the unpredictable environmental influences, such as inadvertent fiber bending. The fibers have a maximal strain tolerance of less than 5%. Although these fibers operated normally following their initial installation in June 2019, anomalies emerged about six months later when the experiment commenced. During this time, some fiber sensors began displaying missing data and aberrant values (falling outside the physically plausible range of 15 to 100°C). This behavior was likely attributed to the substantial impacts of the creeping of the rock formation. Following a calibration process using thermocouple data, the anomalous readings were excluded and substituted with the mean value of their nearest neighboring data points. As anticipated for heat conduction within solids, temperature alterations exhibited relatively gradual changes in comparison to the sampling rate. As such, data were stacked to form hourly averages to reduce memory usage as well as to improve the signal-to-noise ratio of the data.

Figure 6 illustrates the processed temperature measurements recorded by DTS from 21 January 2020 (when heating started) to 15 February 2020 (the first heating event stopped on 18 February 2020). The temperature sensors exhibited robust performance with some minor issues. As depicted in Figure 6b, the 10-m temperature fiber displays instances of missing data (designated as NaN). These gaps exhibit a dual nature of periodicity: they manifest both as temporal periodicity and spatial periodicity, particularly after the initial 5 m of the fiber. Conversely, the 5-m temperature sensor reveals comparatively minimal data loss patterns, except for the outset of the fiber. Further inquiry is warranted to elucidate the underlying cause behind this periodic occurrence of data gaps.

Furthermore, the temperature measurements exhibit numerous abrupt transitions and sudden deviations. These shifts are particularly conspicuous within the 5-m temperature fiber measurements (Figure 6a). Given that the DTS fiber was enclosed within a narrow tube, effectively shielding it from external strain and formation deformation, the occurrence of these sharp shifts and jumps could potentially be attributed to movements of the fiber within the tube. These fluctuations might potentially arise as consequences of minor shifts in location readings.

The temperature data from both fibers are consistent with the experiment setup (shown in Figure 1b): The 0.5-m length heater is located between 2.6 and 3.1 m depth inside the salt formation. The temperature increased significantly on the first day due to the activation of the heater, and then gradually approached a stable state during the remaining 25 days. The location of the heater is clearly shown in both DTS data sets. The small location offset between the two DTS data is due to the deployment difference between the two fibers in the respective boreholes. The spatial relation between the two DTS boreholes is shown in Figure 1b. As is shown in Figure 6, because the 5-m DTS borehole is closer to the heater borehole than the 10-m DTS borehole, the temperature of the 5-m borehole increased more significantly. Assuming the salt around the heater borehole is close to homogeneous (at least for thermal properties), the 1-D temperature measurements from the fibers can be “wrapped around” the heater borehole, rendering a simplified 3-D view profile (Figure 7). As is shown in Figure 7, even though there is only a 0.03-m distance difference from the heater borehole to the 5-m DTS borehole and the 10-m DTS borehole, the temperature difference between the two DTS boreholes is still apparent, indicating rapid temperature decay in the salt formation. Similarly, also indicated in both Figures 6 and 7, the temperature decreases rapidly along both DTS boreholes when moving away from the heater level.

Table 1
Thermal, Hydrological, and Mechanical Parameters Used in the Simulation

Parameters	Value
Grain density (kg m^{-3})	2,200
Young's modulus (Pa)	1.67×10^8
Poisson's ratio	0.37
Tensile Strength (Pa)	2.7×10^{10}
Cohesion (Pa)	3.5×10^{10}
Particle heat capacity ($\text{J kg}^{-1} \text{K}^{-1}$)	860
Particle thermal conductivity ($\text{W m}^{-1} \text{K}^{-1}$)	4
Particle thermal expansion coefficient (K^{-1})	4.0×10^{-5}
Porosity (%)	0.46
Brine saturation (%)	90
Permeability (m^2)	5×10^{-19}
Fluid bulk modulus (Pa)	2.2×10^9
Fluid density (kg m^{-3})	997
Fluid viscosity (Pa s)	0.001
Fluid heat capacity ($\text{J kg}^{-1} \text{K}^{-1}$)	4,181.7
Fluid thermal conductivity ($\text{W m}^{-1} \text{K}^{-1}$)	0.65
Fluid thermal expansion coefficient (K^{-1})	2.0×10^{-5}

3.2. ERT Measurements at WIPP

The collected ERT data underwent a filtering process to eliminate outliers, including data points with unusually high or low values. Following this, the gaps in data were filled through interpolation using an inverse distance approach, and these newly interpolated points were assigned a relatively high measurement error. This was done to maintain a consistent count of measurements throughout the data set. The open-source inversion code, E4D (T. C. Johnson et al., 2010), was used for both optimizing survey design as well as the inversion on the High-Performance Computing facility of Lawrence Berkeley National Laboratory (LBNL). Examples of the inverted ERT data sets showing the change of the formation resistivity during the first 21 days after the heating are shown in Figure 8.

The thermocouple measurements and the resistivity inversion results of three locations, from 21 January to 15 February 2020, are shown in Figures 9b and 9c. The locations of the measurements, with the interval of 1.2 m, are from the depths of 1.7, 2.9, and 4.1 m, respectively (indicated in Figure 9a). Combining the DTS measurements (Figure 9a) and the experiment design (Figure 1b), the measurement at the depth of 2.9 m is the heater level. For the other two locations, the one at 1.7 m depth is slightly closer to the heater (about 0.3 m closer) than the measurement at 4.1-m depth. This spatial relation is also consistent with the thermocouple measurements from the ERT boreholes: The temperature measurements from the 1.7 m depth are slightly higher than the measurements from the 4.1 m depth (Figure 9b). Like the DTS measurements, as is shown in Figure 9b, the temperature increased rapidly during the first day (around 13°C increase at the heater level), then gradually and slowly increased (about 5°C increase at the heater level) during the following 25 days.

It is known that the empirical relationship between temperature change and resistivity is that one-degree temperature change is typically associated with a few percent change in resistivity (Hayley et al., 2007; Revil et al., 1998). The relationship between bulk electrical resistivity and temperature changes can be explained

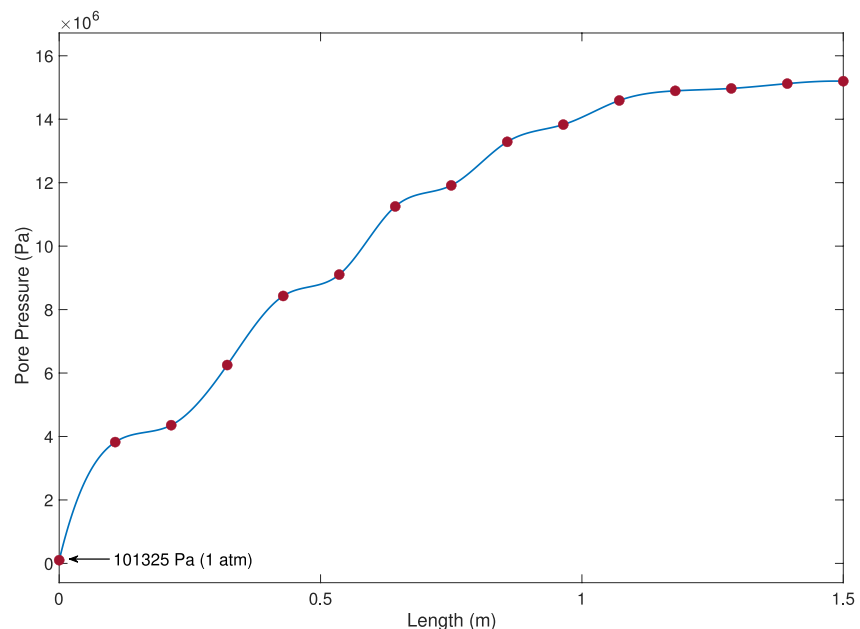


Figure 5. Pore pressure gradient with respect to the distance from the heater borehole after equilibrium from the initial boundary condition and before the start of the heating experiment.

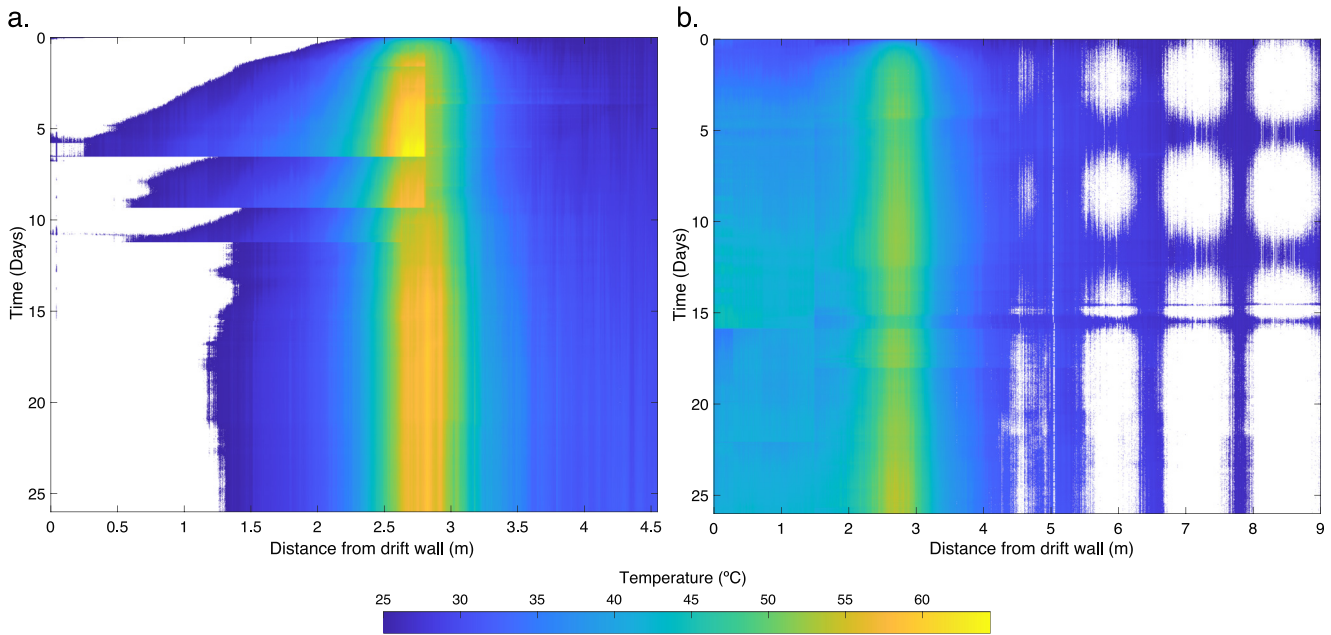


Figure 6. Distributed temperature sensing (DTS) measurements from 21 January to 15 February 2020, at Waste Isolation Pilot Plant. The locations of two DTS boreholes are indicated in Figure 1b (a) Temperature profile from the 5-m DTS borehole. (b) Temperature profile from the 10-m DTS borehole. The white areas indicate invalid data.

by effective medium theory, which is based on infinitely resistive matrix immersed in the conductive medium (Bussian, 1983; Revil et al., 1998). Changes in the electrical resistivity with temperature are due to changes in the fluid viscosity (conduction through pore fluid) (Hayley et al., 2007). The linear effective medium model modified from Hayashi (2004), Hayley et al. (2007) can be written as:

$$\frac{R^T}{R^{25}} = 1 - a(T - 25), \quad (2)$$

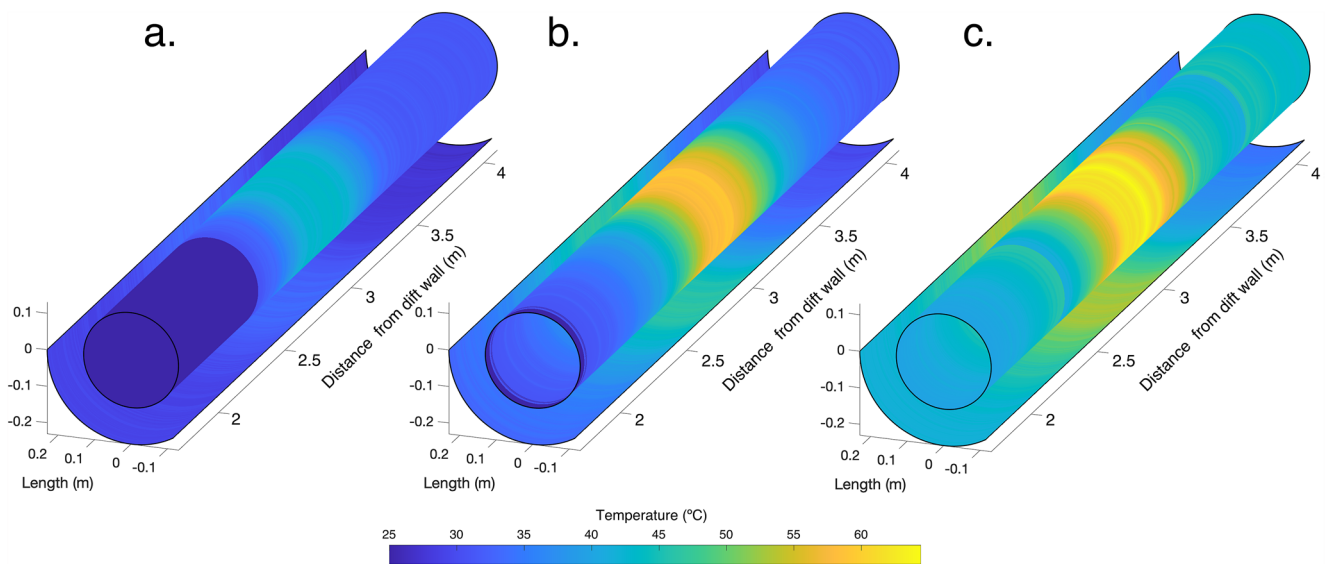


Figure 7. Time-lapse 3-D “wrapped around” view of the distributed temperature sensing (DTS) measurements from 21 January to 15 February 2020. The radii of the “wrapped around” are from the distances between the center of the heater borehole to the two DTS boreholes (indicated in Figure 1). (a) Temperature profile of the second hour. (b) The temperature profile of the 25th hr (c) The temperature profile of the 624th hr (26th day). The dark blue color indicates invalid data.

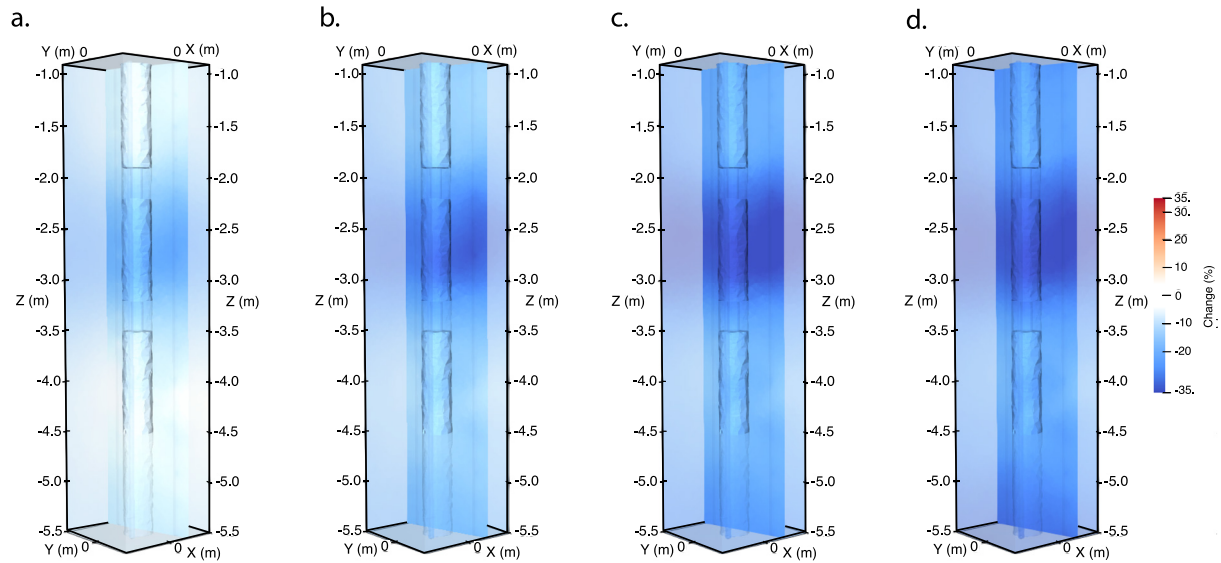


Figure 8. 3D resistivity models show the resistivity change on the first (a), third (b), seventh (c), and the twenty-first (d) days, respectively.

where R^T is the resistivity at temperature T (in Celsius), R^{25} is the resistivity at 25°C , and a is a linear fractional factor that relates resistivity change to temperature change. Previous studies (Hayley et al., 2007; Revil et al., 1998) found the linear coefficient (factor a in Equation 2) between resistivity and temperature is about 0.023 for pore fluid conduction within the $25\text{--}200^\circ\text{C}$ range. Thus, by applying a simple 2% temperature coefficient (Hayley et al., 2007) to the measured temperature data from the ERT boreholes, we can estimate resistivity variation that is solely due to temperature change during the heating process. As is shown in Figure 9c,

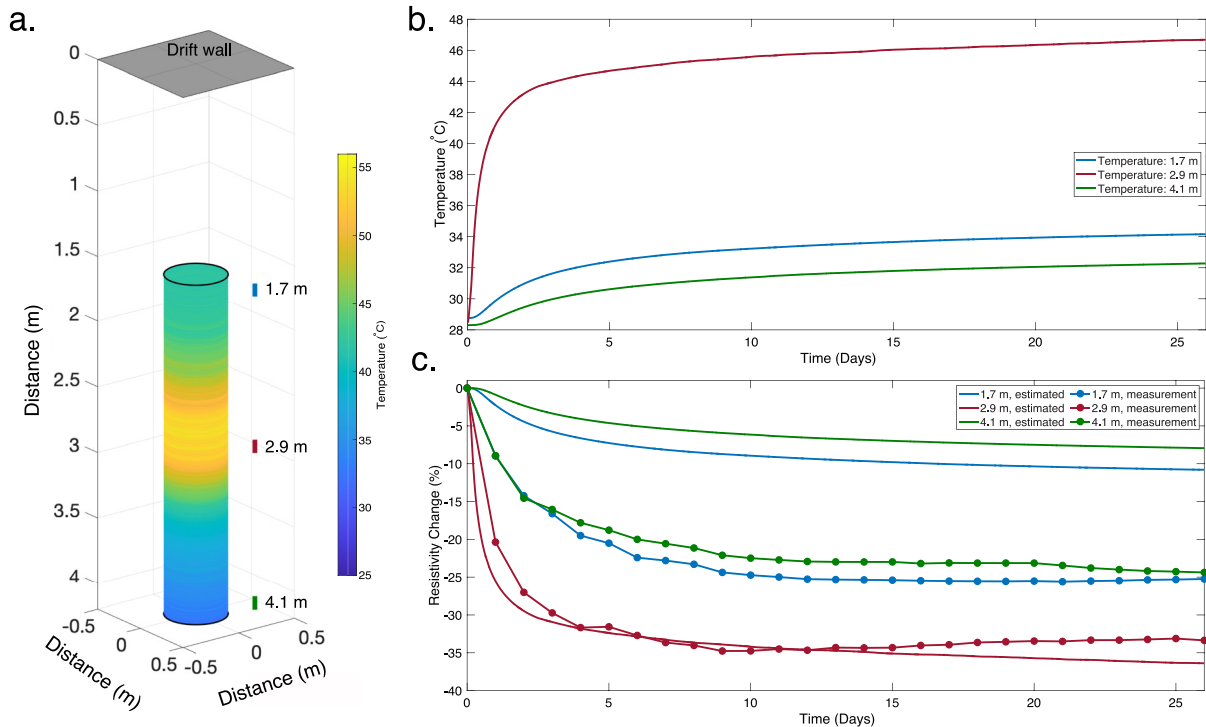


Figure 9. Temperature and resistivity change from 21 January to 15 February 2020. Temperature and resistivity changes are given for different depths along the horizontal borehole. (a) The spatial locations of the three thermocouple measurements and their distance to the center of the heater. The green line segments illustrate thermocouple locations. Like Figure 5, the “wrapped around” temperature profile is from the 5-m temperature fiber optic borehole. (b) Temperature measurements from the thermocouple inside the electrical resistivity tomography (ERT) borehole. (c) Both estimated and measured resistivity changes along the ERT borehole.

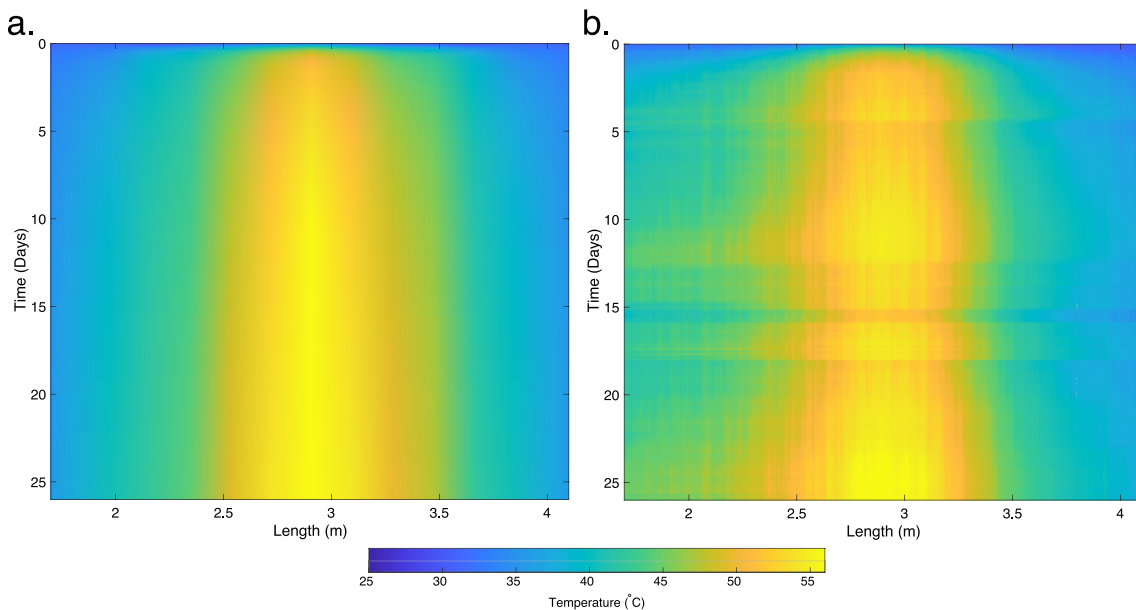


Figure 10. Comparison between (a) the numerical modeling results and (b) the first 5 m of the 10-m distributed temperature sensing measurements at Waste Isolation Pilot Plant from 21 January to 15 February 2020.

the estimated and measured resistivity changes are in good agreement at the heater level (2.9-m deep from the drift wall). However, at the locations that are around 1.2 m away from the heater level (at the locations of 1.7 and 4.1 m from the drift wall), there are significant discrepancies between the measured resistivity changes and the predictions, namely a much more significant decrease in resistivity was observed than was predicted solely from temperature effects. This suggests that, besides temperature, other processes are contributing to the observed resistivity changes during the heating experiment. These possible processes are likely the coupled THM processes that include the brine migration due to thermal pressurization that is triggered by the heating during the experiment. We explore these possible contributing factors with the DEM model discussed below.

3.3. Numerical Simulation Results

Figure 10 shows the comparison between the DTS measurements from the first 5 m of the 10-m DTS borehole and the numerical modeling results. As stated before, we focus on the data from the 10-m DTS borehole due to its better overall quality. Despite the temperature shifts in the DTS measurements due to the formation deformation around the fiber, the numerical simulation result agrees with the DTS measurements reasonably well. Figure 11 shows the comparison between thermocouple measurements from the ERT borehole and the numerical modeling results. The thermocouple 1.7 m from the drift wall is equivalent to 1.05 m from the center of the heater array in the numerical model.

Similarly, the thermocouple 4.1 m from the drift wall corresponds to 1.35 m from the center of the heater array in the numerical model. For better comparison, the locations of the sensors from the numerical modeling results are adjusted and displayed to the corresponding sensor depths at the WIPP. As we can see, the numerical simulation results agree with the actual thermocouple measurements.

4. Discussion

As shown in Figure 9c, the ERT measurements from the in situ heating experiment at WIPP show that the resistivity near the heater agrees with the estimation based on a simple linear temperature-resistivity relationship (Hayley et al., 2007). However, in the cooler regions at around 1.2 m away from the heater level, the resistivity reduces significantly more than the temperature-only based estimations. Multiple additional factors can contribute to this discrepancy, which will be discussed below.

The temperature changes may affect the salinity and resistivity of the pore water in the formation due to its effects on salt solubility, therefore contributing to the discrepancy between the measurements and the estimations.

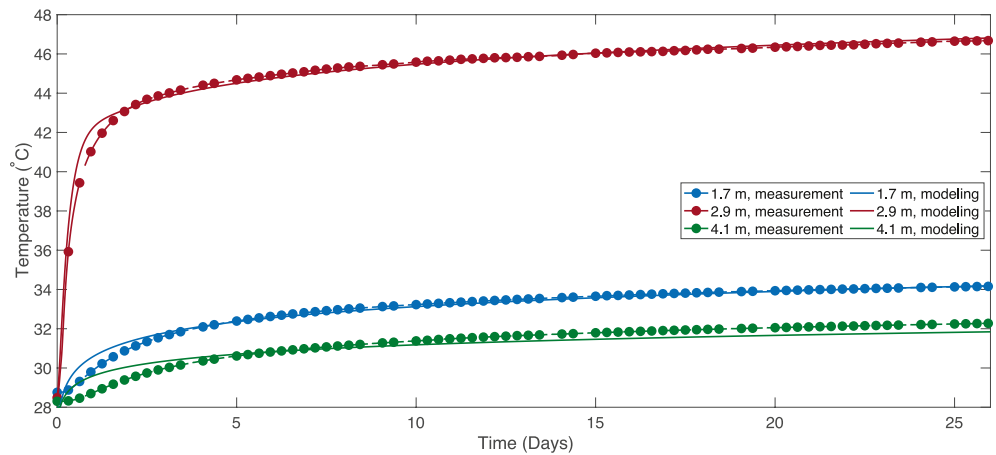


Figure 11. Comparison between the numerical modeling results and the thermocouple measurements from the electrical resistivity tomography borehole from 21 January to 15 February 2020. The dotted lines are measurements. The solid lines are numerical modeling results.

However, because NaCl, the dominant composition of the salt formation at >95%, has a solubility that is less sensitive to temperature changes (Speight, 2017), the temperature change during the experiment has a minimal effect (less than 3%) on the salinity and resistivity of the NaCl saturated brine. Therefore, the contribution from salt solubility variation to the overall conductivity changes of the formation is likely negligible in this field experiment. Beyond salt solubility, this large discrepancy between estimated and observed resistivity changes could also be related to the possible increase of brine saturation, which can have a great impact on the overall conductivity of the formation. However, it is unclear why temperature alone can well explain the resistivity measurements near the heater, but fail to do so at 1.2–1.3 m away from the heater (Figure 9c). We will combine the DEM simulation results, the geophysical measurements, and the previous studies to better understand the pore space micro-mechanics, impacts on the possible brine migration during the heating, and the subsequent impact on the geophysical signals.

The porosity of salt in the EDZ, where these tests were completed, is almost entirely fracture porosity (in comparison, the porosity of the undamaged salt is very small, ~0.01%). The conceptual model is that thermal expansion of the fractured rock salt around the heater closes the fracture porosity and consequently increases the pore pressure during heating. Therefore, the areas with higher temperature increases will likely have a more significant porosity decrease and pore pressure increase, and smaller temperature rises will have lower pressures. Consequently, it is possible that the brine will move from the hotter area into the cooler area due to thermal pressurization. During the BATS experiments, the heater borehole wall has the highest temperature. Because the heater borehole is maintained at a constant pore pressure of 1 atm, brine very close to the heater can flow to the heater borehole without increasing pore pressure there. As a result, the hottest area may have a resistivity increase due to the brine loss in the formation, which counters the temperature effects that cause the resistivity to decrease. In addition, the closing of fractures in the salt, caused by the thermal expansion, may seal the conductive fracture networks, block the brine migration pathways, reduce the overall brine content, and consequently lead to higher resistivity. Therefore, in the ERT borehole, for the hotter area near the heater (2.9 m from the drift wall), we may expect to see resistivity increase comparing to the baseline. On the other hand, in the cooler areas further away from the heater (such as 1.4s or 4.1 m from the drift wall in the ERT borehole), the observed resistivity change would include effects of both brine migration from the hotter area causing resistivity decrease and the thermal expansion of the salt causing resistivity increase. In addition, salt creep is a possible contributing mechanism. However, the short length of the heater test and previous laboratory studies of the WIPP salt (Brodsky & Munson, 1991) indicate that salt creep has little effect on bulk material properties.

In addition to closing cracks between salt grains, temperature increase causes thermal expansion of the brine, which competes with the expansion of salt grains and could lead to pore space enlargement, creation of new fractures (if fluid pressure exceeds the least principal stress), and consequently reduce the resistivity of the salt formation. Furthermore, the pore pressure changes due to the thermal expansion of the brine could move the brine from the hotter area adjacent to the heater into the further cooler area or the heater borehole due to the

open boundary condition. In the hot area close to the heater, the brine content may be stable due to the dissipation of excess pore pressure into the nearby open heater borehole. However, the brine in the salt formation may increase in the further cooler area due to brine migration from the hotter area. As conceptually described above, multiple simultaneous THM processes impact the salt deformation and brine migration that could result in the observed geophysical signals at the WIPP. Mechanistic exploration of these processes using the DEM model help to identify the dominant effects that drive the observed signals, specifically the discrepancy variations between the observed resistivity signals and the theoretical estimations at the near and the far fields. Our discussion, aided with the DEM model, will focus on the following possible scenarios as the results of heating:

1. The generations of new fractures, which could both increase the brine percentage inside the formation and form more conductive pathways.
2. Enlargement of the existing pore space, as well as the higher brine percentage in the formation, due to the thermal expansion of the pore brine.
3. Brine migration from the hotter to the colder area due to the thermal pressurization.

Previous studies at WIPP (Brodsky & Munson, 1991) and the Avery Island salt mine (Blankenship & Stickney, 1983) showed that the thermal expansion of salt during the active heating process closes the fractures, decreasing the permeability of the salt formation. Subsequently, the bulk resistivity of the salt formation would increase from this effect. On the contrary, the thermal expansion of brine, if confined, could generate new fractures that increase permeability and decrease the resistivity of the salt formation (Stesky, 1986). Due to these counteractive processes between the thermal expansion of brine and rock salt matrix, and their respective effects on the resistivity of the formation, fluctuations in the resistivity measurements are expected (Stesky, 1986). However, rather smooth, instead of fluctuating, resistivity changes are observed during the heating experiment in this study (Figure 9c).

To explore the effects more, if temperature increase leads to generations of new fractures and the subsequent increase of brine percentage in the salt formation, the hotter area should exhibit a more significant resistivity decrease, and the cooler areas a smaller resistivity decrease. This contradicts the observed resistivity measurement shown in Figure 9c, which suggests that new fracture creation during heating is unlikely a dominant effect. On the other hand, another possible scenario is that the thermal expansion of the brine overcomes the thermal expansion of the rock salt during the heating. As a result, the growth of the pore space would lead to an increased percentage of brine and, consequently decrease in resistivity of the salt formation. Both the WIPP measurements (Figure 9c) and our DEM simulations suggest that this is an unlikely scenario. Figure 12 shows the numerical simulation results of the changes in salt grain size (particle radius) and the porosity along the ERT borehole (location indicated in Figures 4b and 9a). Because the magnitude of the changes is small, we plot them in percentage. As is shown, both the grain size and the porosity changes are minimal, <0.06% increase of grain size, and a 0.18% decrease in porosity, respectively. These numerical simulations suggest that the volumetric variation of the salt matrix, and porosity, during the heating experiment is negligible. Considering the resistivity changes in the cooler regions from the ERT measurements (the 1.7-m and the 4.1-m curves in Figure 9c) are about five times lower than the theoretical estimations from temperature alone, it is unlikely that the small volumetric changes of grain and porosity are major contributors to the observed resistivity variations away from the heater.

In contrast to small grain size and porosity changes, the DEM simulation shows substantial pore pressure changes during heating (Figure 13). The hottest area has pore pressure increase by 70%, indicating a potential strong driving force, due to the pore pressure gradient, for intergranular brine migration, which could consequently cause resistivity changes. The previous meter-scale laboratory heating test analyzed by Roedder and Belkin (1980) on Salado bedded salt indicated that the intragranular brine contributes little to the brine movement. Post-test mineralogical analysis indicated brine inclusions did migrate in the portions of the salt block nearest to the heater, but rarely across grain boundaries (Lambert, 1980). Meanwhile, the in situ salt dome heating tests at Avery Island (Jenks & Claiborne, 1981; Krause, 1983) suggested the intergranular brine transport is mainly influenced by the pressure gradient—the thermo-poroelasticity model of McTigue (1986, 1990). Combining our current DEM simulation results and previous studies, it is most likely that the dominant process is thermal pressurization driving intergranular brine migration, which redistributes brine and causes the extra decrease in the observed resistivity measurements.

Considering the ultra-low permeability of the intact salt formation at the WIPP, as well as the high confining pressure (around 15 MPa of confining pressure at the 650-m deep WIPP underground test site), it is proper to

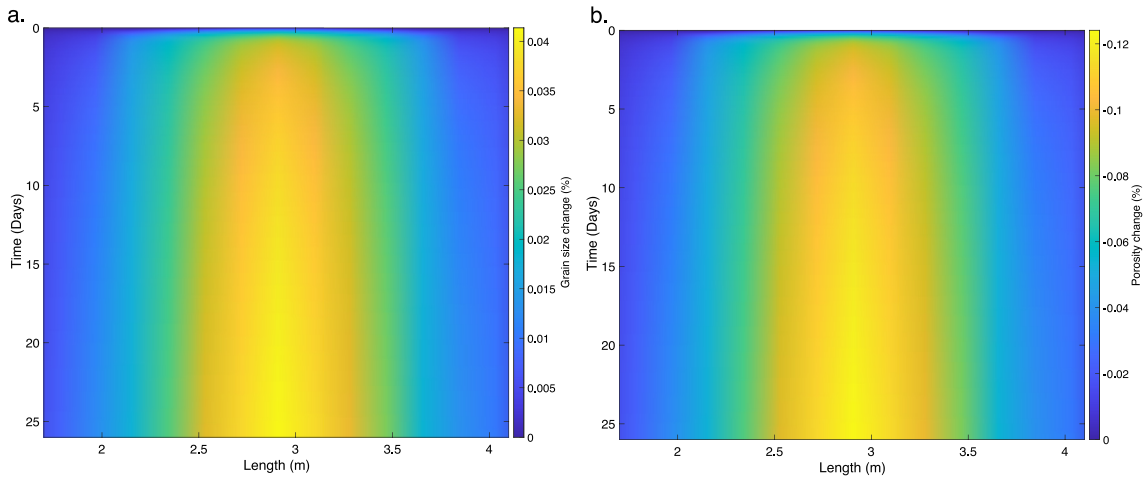


Figure 12. Numerical modeling result of the discrete element model micro-property changes along the electrical resistivity tomography borehole during the heating experiment. (a) Particle radius change percentage. (b) Porosity decrease by percentage.

assume the THM process during the heating is slow and quasi-static, that is, dramatic pore flow and the structural formation changes are very unlikely. Moreover, because of the ultra-low permeability of the salt formation, most brine only migrates a short distance, affecting the neighboring areas.

Figure 14 shows the simulated pore pressure changes over 26 days at the locations of 0.18 and 0.28 m away from the heater borehole, respectively. At the location of 0.18 m from the heater borehole, the pore pressure increases at the early stage of the heating process and gradually decreases due to the dissipation and drainage of excess pore fluid to the nearby open heater borehole. The decrease of the pore pressure suggests continuous drying at the areas adjacent to the heater, which could draw brine in from further areas. Because of the ultra-low permeability of the salt formation, the dissipation process is likely very slow. At the location of 0.28 m from the heater borehole, even only 0.1 m away from the previous location, the pore pressure gradually increases and approaches the stable state after the initial stage of heating, suggesting the influence of the open heater borehole is limited in this location a very short distance away from the heater. This suggests the existence of a possible “boundary” in terms of distance to the open heater borehole where pore pressure increase on the open borehole side of the boundary will lead to brine drainage. In contrast, brine saturation will increase on the other side.

Specifically, in the ERT borehole, the closest observation (2.9-m curve in Figure 9c) is 0.3 m from the heater borehole. Figure 15 shows our conceptual model of the process. At the heater level, the extra pore pressure from

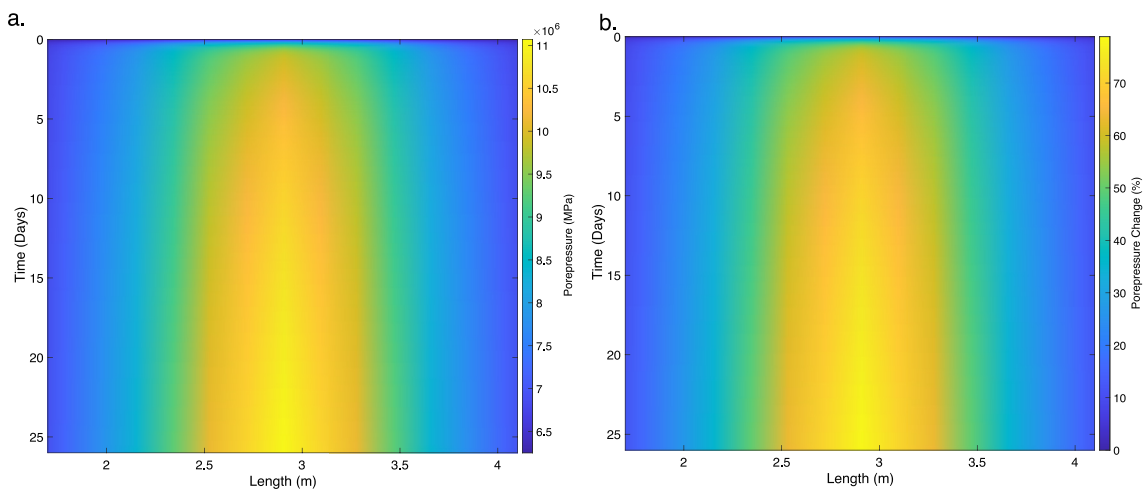


Figure 13. Numerical modeling result of the pore pressure along the electrical resistivity tomography (ERT) borehole during the heating experiment. (a) Pore pressure value along the ERT borehole. (b) Pore pressure change percentile along the ERT borehole.

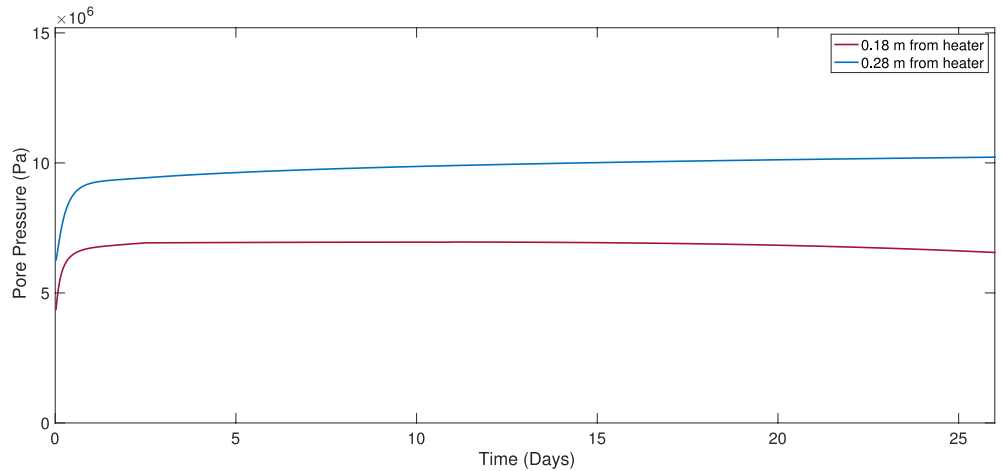


Figure 14. Numerical modeling results of the pore pressure variations at 0.18 and 0.28 m away from the heater borehole, respectively.

thermal expansion likely dissipates toward the open heater borehole where the pressure is ambient, driving brine leakage. This will maintain the brine content near the heater at constant, and as a result, changes of the resistivity

signal are likely dominated by the temperature effects alone. This is consistent with the linear temperature-resistivity correlation observed in this location (Hayley et al., 2007). In the cooler and further regions of the ERT borehole from the heater, the pore pressure variations and the consequent brine migration are influenced by both thermal expansion and the brine migration from the hotter area. This pattern is not exclusive to the salt formation found at WIPP. A comparable phenomenon was identified by Eaton (1972) during efforts to establish an empirical relationship between pore pressure gradient and logging-based resistivity data in the Gulf of Mexico region. They reasoned that the formation easier for water to escape tends to have a smaller resistivity gradient, and vice versa. Despite the contrasting nature of WIPP's salt formation and the sediment in the Gulf of Mexico, there's a striking similarity in the dynamics of brine migration between the two. Because the volumetric changes of the salt matrix are minimal based on the DEM model, as described above, the amount of the brine influx is directly related to the compression magnitude of the preexisting air in the pore. As is illustrated in Figures 15b and 15c, assuming the pore air does not move out of the pore space, the volumetric change of the pore air due to the compression from the brine influx during the heating can be estimated with the basic gas law (Moran et al., 2010):

$$\frac{P_1 V_1}{T_1} = \frac{P_2 V_2}{T_2} \quad (3)$$

where P , V , and T represent the confining pressure, volume, and temperature of the pore air, respectively. The subscripts represent two different stages during the heating process.

Among the three physical quantities in Equation 3, the temperature is directly measured during the experiments at fixed locations. On the other hand, the DEM model can simulate both pore pressure (Figure 13) and temperature (Figure 11) well, as discussed above. Using the temperature from the measurements and the pore pressure from the DEM simulation, subsequently, we can estimate the air volumetric change during the heating by combining the numerical simulation results and the in situ measurements with the gas law.

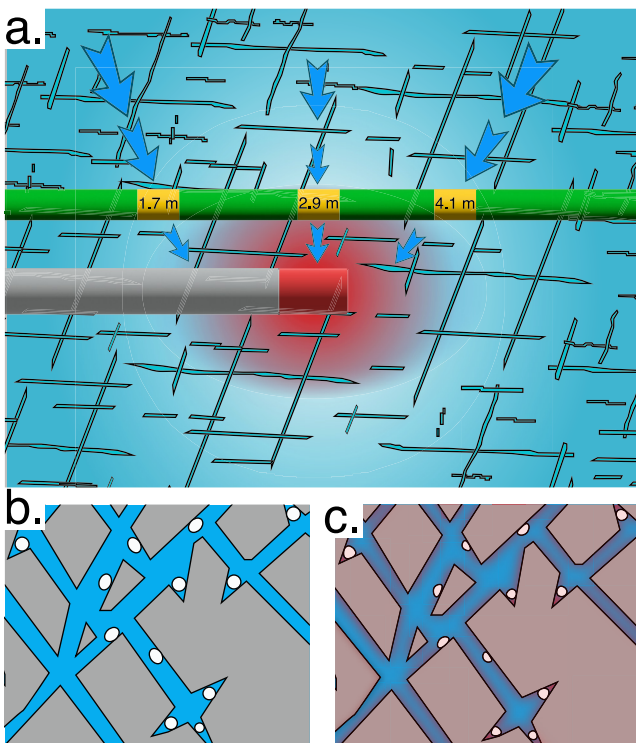


Figure 15. Conceptual diagram of brine migration during the heating process. (a) The overall conceptual diagram of the brine migration process as well as the respective locations of the heater (red zone), electrical resistivity tomography (ERT) borehole (green), and the thermal couples in the ERT borehole (yellow). (b) The schematic diagram of the fracture network in the salt before heating. The blue color represents brine. The gray color represents the salt formation. The white bubbles represent air bubbles. (c) The schematic diagram of the fracture network after heating. The red hue represents the increased temperature. The white bubbles represent the compressed air bubble after heating.

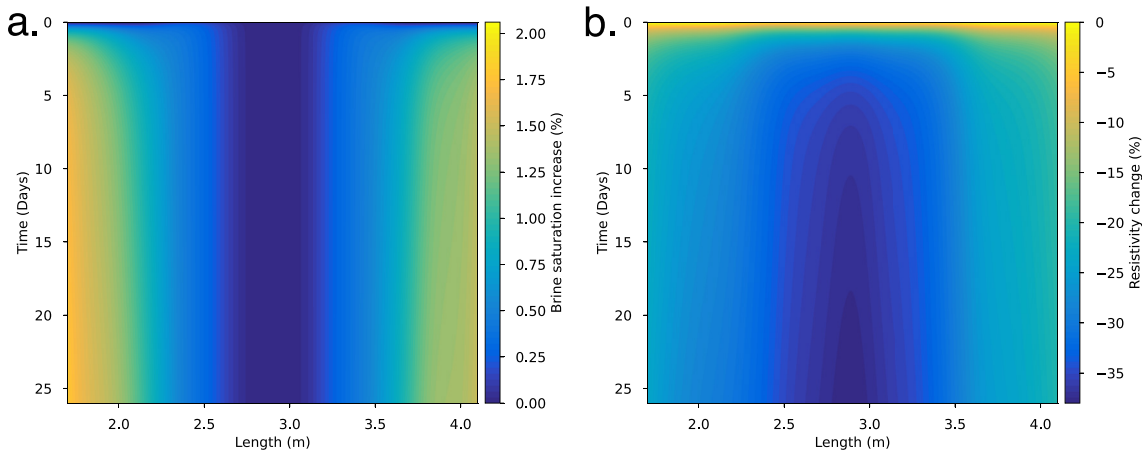


Figure 16. Estimated brine saturation changes (a) and resistivity changes (b) along the electrical resistivity tomography borehole during the heating experiment based on the numerical simulation and the brine migration hypothesis shown in Figure 15.

Assuming air bubble compression is compensated by brine influx, the volumetric change of the air can be approximately equivalent to the brine content increase. By applying Archie's law (Archie, 1942), we can infer resistivity changes of the salt formation from these brine content changes. We used the simplified Archie's law here:

$$R_{\text{rock}} = R_{\text{brine}} \phi S^2, \quad (4)$$

where R_{rock} represents the resistivity of the salt formation, R_{brine} represents the resistivity of the brine, ϕ represents the porosity, S represents the brine saturation. As discussed above, we think the porosity changes during the heating is minimal. So, in this estimation, we consider them as constant. The resistivity of the brine and salt formation is affected by temperature. Combining the temperature effect with this additional brine content increase, we can further estimate the expected resistivity changes and compare them with the measurements during the experiment. The adjusted estimation can be written as:

$$R_{\text{est}} = R(t)(1 + \Delta S^2), \quad (5)$$

where R_{est} is the estimated resistivity, $R(t)$ represent the formation resistivity that is affected by temperature only, ΔS represent the brine saturation changes. Using the numerical simulation and the hypothesis summarized in Figure 15, we can estimate the brine content changes as well as the corrected resistivity estimation during the heating experiment. Here, we used the ERT borehole as an example and showed the results in Figure 16. Extracting the data from the same ERT sensor locations, indicated in Figure 9, we have a much-improved comparison between the new resistivity estimation and the resistivity measurements from the experiment, and shown in Figure 17. There are some remaining discrepancies between the measured and the estimated resistivity changes, which may be due to multiple contributing factors. Among others, this could include (a) the complex microstructure of the fractured salt formation and effects on resistivity that cannot be precisely described by a simple Archie's law, and (b) possible precipitation and dissolution process of the pore brine due to heating that can change ion composition and local pore structure, and (c) the deviation of the simplified pore space composition with no spatial variability, which is likely different from actual site conditions. Nevertheless, the general agreement between the in situ measurements and DEM model-aided estimations suggests that while temperature plays a dominant effect on resistivity near the heater, the resistivity changes in the areas away from the open heater borehole are likely the combined effects of temperature and brine migration driven by thermal pressurization.

5. Conclusions

We conducted a geophysical monitoring campaign during an in situ heating experiment at the underground WIPP facility. Both ERT data and high-resolution DTS data were collected. For the ERT data, the resistivity changes near the heater are likely driven by temperature changes alone. However, the resistivity measurements in regions further away from the heater decrease around five times more than the estimates based on temperature change

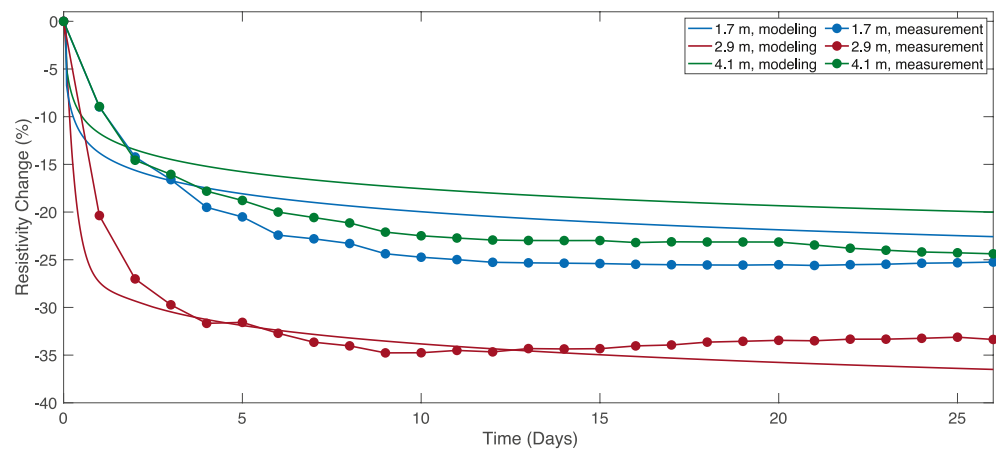


Figure 17. Comparison of the measured and corrected estimated resistivity changes from 21 January to 15 February 2020. The dotted lines are the measurements. The solid lines are the corrected estimations.

alone, indicating other major contributing factors, such as possible generations of new fractures, pore brine salinity increase, or the increase of brine content in the salt formation.

To better understand the mechanism driving these observed geophysical changes, we conducted numerical simulations of the coupled THM process during the experiment using a DEM model. The numerical simulation results show that the magnitude of the grain size and the porosity changes is small, ruling out the effects of porosity changes on resistivity. Consistent with previous studies, numerical simulation results also eliminated the likelihood of new fracture generation and subsequent effects on resistivity changes. On the contrary, the numerical simulation shows substantial pore pressure changes during heating, which leads to thermal pressurization-driven brine movement. Nearest to the heater, the increased pore pressure drives brine into the open heater borehole, which is maintained at atmospheric pressure. As a result, brine is produced in the heater borehole, and the brine content of the formation near the heater likely remains constant or decreases in the long term. Away from the borehole in the cooler area, we infer that the brine content increases due to the compression of existing air bubbles and a lack of drainage. Combining simple gas law, Archie's law, the measurements at the WIPP, and the DEM model, we can estimate the changes of the brine content and its subsequent effect on resistivity jointly with the temperature effect. These improved resistivity estimations agree well with the observed resistivity changes during the experiment, indicating that our interpretation of the brine migration mechanism and the resulting resistivity changes are feasible. We note that our models critically rely on the pore composition, where the trapped air plays a significant role regarding brine content change during heating. This is a valid assumption in our study as the experimental plots are in the EDZ where air entry and brine loss likely occurred before the experiment started. Further into the salt formation, where the disturbance is minimal, and the pore space is near full saturation, the resistivity signals are likely different.

Based on the interpretation of the ERT and simulation responses, we suggest the presence of a pressure “divide” surrounding the heater, separating brine moving toward the heater from brine moving away toward air-filled damage porosity further in the formation. The data presented above suggest that in our experimental setting, this divide is between 0.2 and 0.3 m from the heater borehole. In general, the location of this divide is likely controlled by a combined effect of multiple variables, including the magnitude of temperature change, thermal pressurization, pore saturation, and permeability, among others.

Data Availability Statement

- The open source DEM simulation software, Yade, used in this paper is available at Šmilauer et al. (2021).
- The ERT and DTS data are available at Wang and Wu (2020).

Acknowledgments

Funding for this work was provided by the Spent Fuel and Waste Science and Technology, Office of Nuclear Energy, of the U.S. Department of Energy under Contract Number DE-AC02-05CH11231 with Lawrence Berkeley National Laboratory. Sandia National Laboratories is a multi-mission laboratory managed and operated by National Technology & Engineering Solutions of Sandia, LLC (NTESS), a wholly owned subsidiary of Honeywell International Inc., for the U.S. Department of Energy's National Nuclear Security Administration (DOE/NNSA) under contract DE-NA0003525. This paper describes objective technical results and analysis. This written work is authored by an employee of NTESS. The employee, not NTESS, owns the right, title, and interest in and to the written work and is responsible for its contents. Any subjective views or opinions that might be expressed in the written work do not necessarily represent the views of the U.S. Government. The publisher acknowledges that the U.S. Government retains a non-exclusive, paid-up, irrevocable, worldwide license to publish or reproduce the published form of this written work or allow others to do so for U.S. Government purposes. The DOE will provide public access to the results of federally sponsored research in accordance with the DOE Public Access Plan.

References

Acton, R. U. (1978). "Thermal conductivity of S.E. New Mexico Rocksalt and anhydrite". In V. V. Mirkovich (Ed.), *Thermal conductivity 15*. Springer. https://doi.org/10.1007/978-1-4615-9083-5_33

Archie, G. E. (1942). The electrical resistivity log as an aid in determining some reservoir characteristics. *Transactions of the AIME*, 146(01), 54–62. <https://doi.org/10.2118/942054-g>

Ballentine, C. J., & Burnard, P. G. (2002). Production, release and transport of noble gases in the continental crust. *Mineralogy and Geochemistry*, 47(1), 481–538. <https://doi.org/10.2138/rmg.2002.47.12>

Beauheim, R. L., & Roberts, R. M. (2002). Hydrology and hydraulic properties of a bedded evaporite formation. *Journal of Hydrology*, 259(1–4), 66–88. [https://doi.org/10.1016/S0022-1694\(01\)00586-8](https://doi.org/10.1016/S0022-1694(01)00586-8)

Bettters, C., Vornlocher, J., Paronish, T., Crandall, D., Moore, J., & Kuhlman, K. L. (2020). *Computed tomography scanning and geophysical measurements of the Salado formation from boreholes at the Waste Isolation Pilot Plant (NETL-TRS-1-2020)*. National Energy Technology Laboratory. <https://doi.org/10.18141/1581953>

Blankenship, D., & Stickney, R. (1983). *Nitrogen gas permeability tests at Avery island (ONWI-190(3))*. Office of Nuclear Waste Isolation.

Bradshaw, R. L., & McClain, W. C. (1971). *Project salt Vault: A demonstration of the disposal of high-activity solidified wastes in underground salt mines (ORNL-4555)*. Oak Ridge National Laboratory. <https://doi.org/10.2172/4052488>

Brodsky, N., & Munson, D. (1991). "The effect of brine on the creep of WIPP salt in laboratory tests". In *The 32nd US symposium on rock mechanics, Norman OK, 10–12 July 1991*.

Buchholz, S. A. (2016). Test results and comparison of triaxial strength testing of waste isolation Pilot plant clean salt, United States. <https://doi.org/10.2172/1335755>

Bussian, A. E. (1983). Electrical conductance in a porous medium. *Geophysics*, 48(9), 1258–1268. <https://doi.org/10.1190/1.1441549>

Catalano, E., Chareyre, B., Cortis, A., & Barthélemy, E. (2011). A pore-scale hydro-mechanical coupled model for geomaterials. In *PARTICLES II: Proceedings of the II international conference on particle-based methods: Fundamentals and applications* (pp. 798–809). CIMNE.

Caulk, R., Scholts, L., Krzaczek, M., & Chareyre, B. (2020). A pore-scale thermo-hydro-mechanical model for particulate systems. *Computer Methods in Applied Mechanics and Engineering*, 372, 113292. <https://doi.org/10.1016/j.cma.2020.113292>

Chan, K., Bodner, S., & Munson, D. (1998). Recovery and healing of damage in WIPP salt. *International Journal of Damage Mechanics*, 7(2), 143–166. <https://doi.org/10.1177/105678959800700204>

Eaton, B. A. (1972). The effect of overburden stress on geopressure prediction from well logs. *Journal of Petroleum Technology*, 24(08), 929–934. <https://doi.org/10.2118/3719-pa>

Evangelista, L., de Silva, F., d'Onofrio, A., Di Fiore, V., Silvestri, F., di Santolo, A. S., et al. (2017). Application of ERT and GPR geophysical testing to the subsoil characterization of cultural heritage sites in Napoli (Italy). *Measurement*, 104, 326–335. <https://doi.org/10.1016/j.measurement.2016.07.042>

Evans, T. M., Mojarrad, H., Cunningham, C., & Tayebali, A. A. (2009). Grain size distribution effects in 2D discrete numerical experiments. In *Contemporary topics in in situ testing, analysis, and reliability of foundations* (pp. 58–65).

Faybishenko, B., Birkholzer, J., Sassani, D., & Swift, P. (2017). International approaches for nuclear waste disposal in geological formations: Geological challenges in radioactive waste isolation—Fifth worldwide review, United States. <https://doi.org/10.2172/1353043>

Guiltinan, E. J., Kuhlman, K. L., Rutqvist, J., Hu, M., Boukhalfa, H., Mills, M., et al. (2020). Temperature response and brine availability to heated boreholes in bedded salt. *Vadose Zone Journal*, 19(1), e20019. <https://doi.org/10.1002/vzj2.20019>

Hayashi, M. (2004). Temperature-electrical conductivity relation of water for environmental monitoring and geophysical data inversion. *Environmental Monitoring and Assessment*, 96(1–3), 119–128. <https://doi.org/10.1023/b:emas.0000031719.83065.68>

Hayley, K., Bentley, L. R., Gharibi, M., & Nightingale, M. (2007). Low temperature dependence of electrical resistivity: Implications for near surface geophysical monitoring. *Geophysical Research Letters*, 34(18), L18402. <https://doi.org/10.1029/2007GL031124>

Hess, H. H., Adkins, J. N., Heroy, W. B., Benson, W. E., Hubbert, M. K., Frye, J. C., et al. (1957). *The disposal of radioactive waste on land, report of the committee on waste disposal of the Division of Earth Sciences. (Publication 519)*. National Academy of Sciences-National Research Council. <https://doi.org/10.17226/18527>

IAEA. (2018). *Status and trends in spent fuel and radioactive waste management. (NW-T-1.14)*. International Atomic Energy Agency (IAEA).

Jenks, G. H., & Claiborne, H. (1981). *Brine migration in salt and its implications in the geologic disposal of nuclear waste (ORNL-5818)*. Oak Ridge National Laboratory. <https://doi.org/10.2172/5293582>

Johnson, P. J., Boukhalfa, H., Weaver, D. J., Otto, S., Dozier, B. L., Stauffer, P. H., et al. (2017). *Test plan document for thermal testing in salt. SFWD-SFWST-2017-000043, LA-UR-17-30762*. Los Alamos National Laboratory.

Johnson, T. C., Versteeg, R. J., Ward, A., Day-Lewis, F. D., & Revil, A. (2010). Improved hydrogeophysical characterization and monitoring through parallel modeling and in-version of time-domain resistivity and induced-polarization data. *Geophysics*, 75(4), WA27–WA41. <https://doi.org/10.1190/1.3475513>

Korganbayev, S., De Landro, M., Morra, F., Cigada, A., & Saccomandi, P. (2020). "Fiber optic sensors for distributed and quasi-distributed temperature measurement". In *2020 IEEE sensors* (pp. 1–4).

Krause, W. (1983). *Avery island brine migration tests: Installation, operation, data collection, and analysis (ONWI-190(4))*. RE/SPEC.

Kuhlman, K. L., & Malama, B. (2013). *Brine flow in heated geologic salt (SAND2013-1944)*. Sandia National Laboratories.

Kuhlman, K. L., Mills, M. M., Jayne, R. S., Matteo, E. N., Herrick, C. G., Nemer, M., et al. (2020). *FY20 Update on brine availability test in salt. Revision 4 (SAND2020-9034R)*. Sandia National Laboratories. <https://doi.org/10.2172/1657890>

Kuhlman, K. L., Mills, M. M., & Matteo, E. N. (2017). *Consensus on intermediate Scale Salt field test design (SAND2017-3179R)*. Sandia National Laboratories.

Lambert, S. J. (1980). *Mineralogical aspects of fluid migration in the Salt Block II experiment (SAND79-2423)*. Sandia National Laboratories. <https://doi.org/10.2172/532528>

Lambert, S. J., & Shefelbine, H. C. (1979). *Strategy for investigation of fluid migration in evaporites (waste isolation Pilot plant-WIPP) (SAND79-1889)*. Sandia National Laboratories. <https://doi.org/10.2172/5579788>

Larson, K. W. (2000). Development of the conceptual models for chemical conditions and hydrology used in the 1996 performance assessment for the Waste Isolation Pilot Plant. *Reliability Engineering & System Safety*, 69(1–3), 59–86. [https://doi.org/10.1016/S0951-8320\(00\)00025-9](https://doi.org/10.1016/S0951-8320(00)00025-9)

Lee, W.-H., Zhang, Y., & Zhang, J. (2017). Discrete element modeling of powder flow and laser heating in direct metal laser sintering process. *Powder Technology*, 315, 300–308. <https://doi.org/10.1016/j.powtec.2017.04.002>

Loke, M., Chambers, J., Rucker, D., Kuras, O., & Wilkinson, P. (2013). Recent developments in the direct-current geoelectrical imaging method. *Journal of Applied Geophysics*, 95, 135–156. <https://doi.org/10.1016/j.jappgeo.2013.02.017>

- McTigue, D. F. (1986). Thermoelastic response of fluid-saturated porous rock. *Journal of Geophysical Research*, *91*(B9), 9533–9542. <https://doi.org/10.1029/JB091iB09p09533>
- McTigue, D. F. (1990). Flow to a heated borehole in porous, thermoelastic rock: Analysis. *Water Resources Research*, *26*(8), 1763–1774. <https://doi.org/10.1029/WR026i008p01763>
- McTigue, D. F., & Nowak, E. J. (1987). *Brine transport studies in the bedded salt of the waste isolation Pilot plant (WIPP) (SAND87-1274C)*. Sandia National Laboratories.
- Moran, M. J., Shapiro, H. N., Boettner, D. D., & Bailey, M. B. (2010). *Fundamentals of engineering thermodynamics*. John Wiley & Sons.
- Morra, F., De Landro, M., Korganbayev, S., Wolf, A., Dostovalov, A., Cigada, A., & Saccomandi, P. (2020). Spatially resolved thermometry during laser ablation in tissues: Distributed and quasi-distributed fiber optic-based sensing. *Optical Fiber Technology*, *58*, 102295. <https://doi.org/10.1016/j.yofte.2020.102295>
- Najari, M., & Selvadurai, A. P. S. (2014). Thermo-hydro-mechanical response of granite to temperature changes. *Environmental Earth Sciences*, *72*(1), 189–198. <https://doi.org/10.1007/s12665-013-2945-3>
- Nowak, E., & McTigue, D. (1987). *Interim results of brine transport studies in the waste isolation Pilot plant (WIPP) (SAND87-0880)*. Sandia National Laboratories.
- O'Sullivan, C. (2011). Particle-based discrete element modeling: Geomechanics perspective. *International Journal of Geomechanics*, *11*(6), 449–464. [https://doi.org/10.1061/\(asce\)gm.1943-5622.0000024](https://doi.org/10.1061/(asce)gm.1943-5622.0000024)
- Revil, A., Cathles, L. M., Losh, S., & Nunn, J. A. (1998). Electrical conductivity in shaly sands with geophysical applications. *Journal of Geophysical Research*, *103*(B10), 23925–23936. <https://doi.org/10.1029/98JB02125>
- Reynolds, J. M. (2011). *An introduction to applied and environmental geophysics*. John Wiley & Sons.
- Roedder, E., & Bassett, R. (1981). Problems in determination of the water content of rock-salt samples and its significance in nuclear-waste storage siting. *Geology*, *9*(11), 525–530. [https://doi.org/10.1130/0091-7613\(1981\)9<525:pidotw>2.0.co;2](https://doi.org/10.1130/0091-7613(1981)9<525:pidotw>2.0.co;2)
- Roedder, E., & Belkin, H. (1980). "Migration of fluid inclusions in polycrystalline salt under thermal gradients in the laboratory and in Salt Block II". In *Proceedings of the 1980 national waste terminal storage program information meeting* (Vol. 212, pp. 361–363).
- Scholtès, L., & Donzé, F. V. (2013). A DEM model for soft and hard rocks: Role of grain interlocking on strength. *Journal of the Mechanics and Physics of Solids*, *61*(2), 352–369. <https://doi.org/10.1016/j.jmps.2012.10.005>
- Scholtès, L. U. C., & Donzé, F. V. (2012). Modelling progressive failure in fractured rock masses using a 3D discrete element method. *International Journal of Rock Mechanics and Mining Sciences*, *52*, 18–30. <https://doi.org/10.1016/j.ijrmms.2012.02.009>
- Šmilauer, V., Angelidakis, V., Catalano, E., Caulk, R., Chareyre, B., Chèvremont, W., et al. (2021). *Yade documentation (3rd ed) [Software]*. The Yade Project. <https://doi.org/10.5281/zenodo.5705394>
- Speight, J. G. (2017). *Lange's handbook of chemistry*. McGraw-Hill Education.
- Stauffer, P. H., Jordan, A. B., Weaver, D. J., Caporuscio, F. A., Tencate, J. A., Boukhalfa, H., et al. (2015). *Test proposal document for phased field testing in salt, FCRD-UFDD-2015-000077, LA-UR-15-23154*. Los Alamos National Laboratory.
- Stesky, R. (1986). Electrical conductivity of brine-saturated fractured rock. *Geophysics*, *51*(8), 1585–1593. <https://doi.org/10.1190/1.1442209>
- Stickney, R., & Van Sambeek, L. (1984). *Summary of the Avery Island field testing program (RSI-0225)*. RE/SPEC.
- Stránský, J., & Jirásek, M. (2011). Calibration of particle-based models using cells with periodic boundary conditions. In *PARTICLES II: Proceedings of the II international conference on particle-based methods: Fundamentals and applications* (pp. 274–285). CIMNE.
- Tomac, I., & Gutierrez, M. (2015). Formulation and implementation of coupled forced heat convection and heat conduction in DEM. *Acta Geotechnica*, *10*(4), 421–433. <https://doi.org/10.1007/s11440-015-0400-1>
- Wang, J., & Wu, Y. (2020). WIPP_BATS1_Temperature_Fiber [Dataset]. Zenodo. <https://doi.org/10.5281/zenodo.7850759>
- Wilkinson, P. B., Meldrum, P. I., Chambers, J. E., Kuras, O., & Ogilvy, R. D. (2006). Improved strategies for the automatic selection of optimized sets of electrical resistivity tomography measurement configurations. *Geophysical Journal International*, *167*(3), 1119–1126. <https://doi.org/10.1111/j.1365-246x.2006.03196.x>
- Wuttke, F., Sattari, A. S., Rizvi, Z. H., & Motra, H. B. (2017). Advanced meso-scale modelling to study the effective thermo-mechanical parameter in solid geomaterial. In *Advances in laboratory testing and modelling of soils and shales* (pp. 85–95). Springer.
- Wyllie, M. R. J., & Gregory, A. R. (1955). Fluid flow through unconsolidated porous aggregates. *Industrial & Engineering Chemistry*, *47*(7), 1379–1388. <https://doi.org/10.1021/ie50547a037>